Frontiers in Earth Science

TYPE Original Research
PUBLISHED 18 February 2026
DOI 10.3389/feart.2026.1677805

EDITED BY
Gilda Maria Currenti,
National Institute of Geophysics and Volcanology (INGV), Italy

REVIEWED BY
Joaquin Alberto Cortes,
Edge Hill University, United Kingdom
Sri Budhi Utami,
The University of Queensland, Australia
Deepak Garg,
National Institute of Geophysics and Volcanology (INGV), Italy

*CORRESPONDENCE
H. Albert,
✉ halbert@ub.edu

RECEIVED 01 August 2025
REVISED 13 January 2026
ACCEPTED 21 January 2026
PUBLISHED 18 February 2026

CITATION
Albert H, Torres-González PA, Lamolda H, Villasante-Marcos V, Luengo-Oroz N, Fernández-García A, Molina-Arias AJ, Aulinas M, González-Alonso E, Prieto F, Gisbert G and Troll VR (2026) An interdisciplinary approach to the pre- and syn-eruptive magma dynamics during the Tajogaite monogenetic eruption (La Palma, 2021).
*Front. Earth Sci.* 14:1677805.
doi: 10.3389/feart.2026.1677805

# An interdisciplinary approach to the pre- and syn-eruptive magma dynamics during the Tajogaite monogenetic eruption (La Palma, 2021)

H. Albert[1,2]*, P. A. Torres-González[3], H. Lamolda[4,5], V. Villasante-Marcos[4], N. Luengo-Oroz[3], A. Fernández-García[4], A. J. Molina-Arias[3], M. Aulinas[1,2], E. González-Alonso[4], F. Prieto[4], G. Gisbert[1,2] and V. R. Troll[6,7]

[1]Department of Mineralogy, Petrology and Applied Geology, University of Barcelona, Barcelona, Spain, [2]Geomodels Research Institute, Universitat de Barcelona, Barcelona, Spain, [3]Instituto Geográfico Nacional, Centro Geofísico de Canarias, Santa Cruz de Tenerife, Spain, [4]Instituto Geográfico Nacional, Observatorio Geofísico Central, Madrid, Spain, [5]Research Group 'Geodesia', Universidad Complutense de Madrid, Madrid, Spain, [6]Department of Earth Sciences, Natural Resources & Sustainable Development (NRHU), Uppsala University, Uppsala, Sweden, [7]Instituto de Estudios Ambientales y Recursos Naturales (i-UNAT), University of Las Palmas de Gran Canaria, Las Palmas de Gran Canaria, Spain

The 2021 Tajogaite eruption (La Palma, Canary Islands) provides a unique opportunity to investigate magma dynamics in magmatic systems where developed and monogenetic volcanoes coexist. Here, we present an integrated, interdisciplinary study combining petrological, geochemical, and geophysical data to reconstruct the pre- and syn-eruptive processes that controlled the evolution of the eruption. Whole-rock and mineral chemistry, diffusion chronometry in olivine crystals, gas geochemistry, GNSS, InSAR, seismicity and eruptive column height monitoring were jointly analyzed to constrain magma storage conditions, magmatic processes and the temporal evolution of the plumbing system. Our multidisciplinary results reveal a multi-stage magmatic history, involving at least three pre-eruptive intrusions (2017–2018, 2020, and in the weeks before the 2021 eruption) that progressively revived the system. Olivine diffusion modeling indicates that the 2021 eruption was triggered by a late-stage intrusion in early September, with ascent times of 10–30 days. Throughout the eruption, additional deep magma injections were recorded through changes in crystal chemistry, ground deformation, and eruptive dynamics. The earliest erupted magmas of the 2021 eruption were more evolved and hosted olivine crystals with oscillatory zoning, reflecting conduit opening and rapid ascent. During the second half of the eruption, the system transitioned to a regime marked by the development of a crystal mush zone, where magma accumulated without immediate eruption. This evolution was evidenced by prolonged olivine residence times and a characteristic 5-day lag between deformation peaks and maximum eruptive column heights during this period. Therefore, to further improve eruption forecasting in monogenetic systems and to resolve the formation of transient magma storage zones in the upper crust that might control the eruption dynamics, we highlight the critical importance of integrating petrological and geophysical monitoring.

KEYWORDS

**diffusion chronometry, La Palma (Canary Islands), monitoring, monogenetic volcanism, olivine, Tajogaite, volcanic hazards**

## 1 Introduction

Forecasting volcanic eruptions is usually concerned with three challenging questions: when, where, and how will an eruption occur? These questions are often approached independently due to the high specialization and limited perspective of any single discipline but might profit from an integrated multi- and interdisciplinary approach to disentangle the correlations existing between results from different disciplines and thus increase confidence in emergency planning and decision making at times of volcanic crisis. This article focuses on applying an interdisciplinary petrological, geochemical, and geophysical approach to improve the forecasting of future unrest and changes in eruption dynamics during monogenetic eruptions by using the 2021 La Palma (Tajogaite) eruption as a case study.

Compared to frequently erupting volcanoes, the scientific understanding of monogenetic fields is limited due to the diverse types of eruptions and the scarcity of witnessed eruptions in these volcanic systems. In fact, monogenetic volcanic fields, which can remain potentially active for millions of years, usually have short periods of magmatic unrest and activity compared to long relatively periods of inactivity (Kereszturi and Németh, 2012). Precisely predicting pre-eruptive timescales of unrest remains a significant challenge in volcanology, as monogenetic eruptions may occur with limited or no warning after variable periods of unrest, which can differ from case to case (e.g., Paricutin volcano; Luhr et al., 1993, and recent Icelandic fissure eruptions; Caracciolo et al., 2023; Kahl et al., 2023). Successful forecasting relies on the ability to interpret monitoring data and identify eruption precursors showing consistent changes from normal background levels of activity. Traditional monitoring techniques include geophysical, geodetic, and gas and water geochemistry methods for measuring seismic activity, ground deformation, gas emissions and changes in groundwater composition (Carbone and Greco, 2007; Nagaoka et al., 2012; Aoki et al., 2013; Cannavò et al., 2015; López et al., 2017; Torres-González et al., 2020; Reath et al., 2021). Recently, and due to its potential in identifying magma arrests and/or mixing at depth that can lead to changes in eruptive behaviour (Kahl et al., 2011; Pankhurst et al., 2018; Albert et al., 2019; Re et al., 2021; Mangler et al., 2022), petrology has also been included during ongoing eruptions as an important monitoring technique (Cashman and Taggart, 1983; Luhr and Carmichael, 1990; Saunders et al., 2012; Reubi et al., 2019; Liu et al., 2020; Berthod et al., 2021; Re et al., 2021; Bindeman et al., 2022; Corsaro and Miraglia, 2022). For this purpose, a detailed and consistent sampling during the eruption is mandatory (e.g., Day et al., 2022b; Ubide et al., 2023; Longpré et al., 2025).

To answer the questions of when, where, and how a monogenetic eruption will occur, it is necessary to understand not only the tectonic regime, but also the structure of the upper crust and how the new intruding magma will interact with it. This requires an inter- and multidisciplinary methodology capable of providing a comprehensive spatial and temporal model. This model should address how the crust structure and the absence or presence of previously emplaced magma bodies will influence the dyke path trajectory, and consequently: (i) the timescales of unrest preceding the eruption, (ii) the trajectory of the shallow dyke and the final location of the eruption, and (iii) the eruptive style and its changes through time, also related to syn-eruptive magma arrest and/or mixing at depth.

Through the study of the emitted materials during a monogenetic eruption, petrological and geochemical studies provide evidence of the thermodynamic conditions of magma storage such as temperature, oxygen fugacity, and pressure, which can be translated into depth. Moreover, petrology provides information on the plumbing system's architecture by recording magma arrests and interactions with previously emplaced magma bodies, and magma dynamics via e.g., diffusion chronometry models on the crystals that allow calculating the timescales of the magmatic processes (Blundy and Cashman, 2008; Kahl et al., 2011; Albert et al., 2015; Albert et al., 2019; Albert et al., 2020; Albert et al., 2022; Cashman and Edmonds, 2019; Edmonds et al., 2019; Ubide et al., 2019; Larrea et al., 2021; Petrone and Mangler, 2021).

Furthermore, monitoring surveys including gas geochemistry, seismicity and geodesy may offer complementary views of the state and temporal evolution of the magmatic system, providing crustal models that reveal the spatial distribution of magmatic bodies at depth and variations in the system conditions (Malengreau et al., 1999; Fernández et al., 2002; Gottsmann et al., 2008; Barde-Cabusson et al., 2014; García-Yeguas et al., 2017; López et al., 2017; Miller et al., 2017; Dumont et al., 2019; Torres-González et al., 2019; Torres-González et al., 2020; Troll et al., 2024b). The integration of all these data and results can potentially lead to the identification of pre-eruptive signals and unrest patterns for each monogenetic field, allowing for the discernment of unrest episodes that will or will not lead to an eruption in the future.

The eruptive style can change over time during an eruption due to variations in magma supply, gas release, and syn-eruptive changes in the volcanic plumbing system (Cassidy et al., 2018). These changes may manifest as transitions between explosive and effusive eruptive phases, shifts in eruption intensity, or alterations in the vent configuration. In this study, we propose the identification of precursors to changes in the eruptive style during the Tajogaite eruption through a detailed chronological analysis of the eruptive style, the eruptive column height, the erupted deposits (petrological and geochemical studies), and the geophysical, geodetic and geochemical monitoring signals.

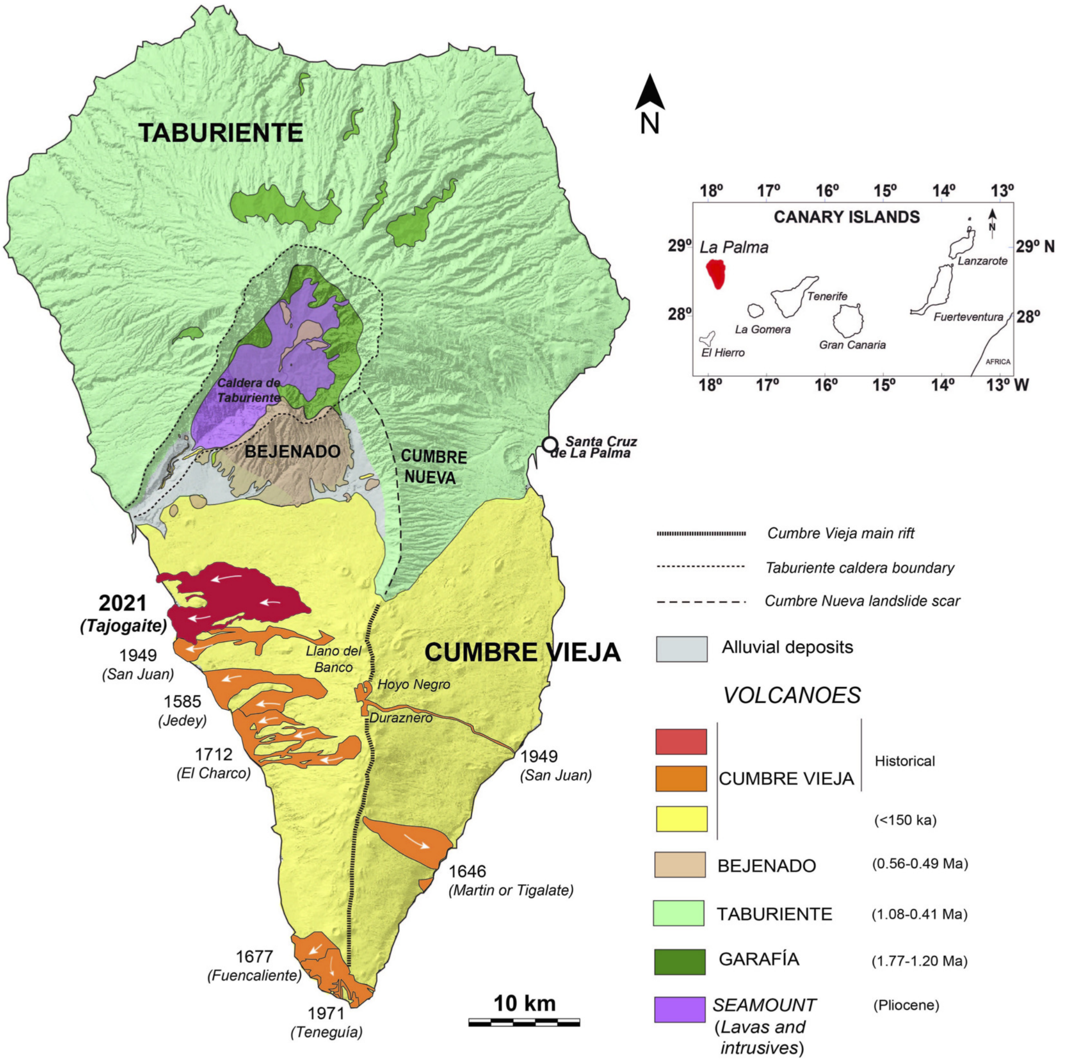

FIGURE 1
Geological map of La Palma showing the main volcanic edifices and formations, as well as the locations of historical eruptions. The map highlights the principal structural features, including the Cumbre Vieja rift zone, the Cumbre Nueva landslide scar, and the Taburiente caldera boundary. The inset shows the location of La Palma within the Canary Islands archipelago. Modified from Carracedo and Troll (2016).

## 2 Geological setting

La Palma is the north-westernmost of the Canary Islands, with an area of 706 km$^2$ and reaching 2,430 m above sea level (m.a.s.l.). The island extends along a N-S axis and comprises two main volcanic units: the Taburiente domain in the north and the Cumbre Vieja monogenetic volcanic field in the south (Figure 1).

The initial stage of La Palma's formation involved an early submarine stage, creating La Palma Seamount Series dated to the Pliocene (3–4 Ma) based on foraminifera (Staudigel and Schmincke, 1984; Staudigel et al., 1986; Tauxe et al., 2000). This seamount, formed primarily of pillow breccias, pillow lavas, and hyaloclastites, developed at depths between 4,000 and 1,800 m below sea level (m.b.s.l.), and was associated with metasomatism of the lithospheric mantle (Carracedo et al., 2001; Klügel et al., 2017). A significant hiatus marked the transition from submarine to subaerial volcanism (Carracedo et al., 2001; Guillou et al., 2001).

Subaerial volcanic activity began approximately 1.8 Ma on the northern side of the island, leading to the formation of the Garafía volcano, which collapsed partially 1.2 Ma ago towards the southwest (Ancochea et al., 1994). This collapse created a depression that was subsequently filled by intense volcanism, forming the Taburiente volcano, an edifice 25 km in diameter and approximately 3,000 m in height (Carracedo and Troll, 2016). The Taburiente volcano's eruptions transitioned from mafic to felsic compositions, indicating magma evolution from basaltic to more differentiated types (Carracedo and Troll, 2016).

In the advanced stages of Taburiente's development, volcanic activity migrated southward, culminating in the Cumbre Nueva edifice. This volcano experienced a significant landslide on its western flank 560 ka ago, creating the Valle de Aridane and leading to the growth of the Taburiente Caldera (Carracedo et al., 2001). The resulting caldera, an eroded structure, exposes part of the uplifted submarine edifice (Ancochea et al., 1994). From the landslide deposits, the Bejenado volcano was formed, and after a period of quiescence, volcanic activity resumed around 123 ka ago, forming the Cumbre Vieja volcanic rift to the south (Figure 1).

Cumbre Vieja represents the most active monogenetic volcanic field in the Canaries (Carracedo and Troll, 2016). Its vents are primarily located along a 20 km north-south rift, reaching up to 1950 m.a.s.l. All La Palma documented historical eruptions, occurred in 1470, 1585, 1646, 1677, 1712, 1949, 1971, and 2021 CE, have taken place along this rift (Romero Ruiz, 1990; Carracedo et al., 2022).

The geological evolution of La Palma involves intricate processes of magma storage and differentiation. Mineral-melt barometry studies indicate that magma was stored at shallower depths in the Bejenado and Cumbre Vieja units (500–800 MPa, 16–26 km) compared to the Taburiente units (1,170 MPa, 40 km), suggesting the development of a magma pooling system (Galipp et al., 2006; Klügel et al., 2017). The variation in major and trace elements is primarily explained by fractional crystallization models, though changes in factors such as oxygen fugacity, pressure of magma storage, and $H_2O$ activity are also noted (Klügel et al., 2017).

## 2.1 Recent volcanism on La Palma: the 20th century eruptions

La Palma experienced two significant volcanic eruptions in the 20th century, occurring in June 1949 and October 1971 (Hernandez-Pacheco and Valls, 1982; Carracedo et al., 2001).

The 1949 eruption, known as the San Juan eruption, involved three eruptive centres: Llano del Banco, Duraznero and Hoyo Negro (Figure 1). Precursory seismic activity was felt up to two and a half years prior to the eruption, intensifying from 3 months before the eruption (Albert et al., 2016). By March of the same year, the seismicity was intense enough to cause property damages and created E-W oriented fissures in the terrain (Klügel et al., 1999). The eruption, which lasted from June 24 to July 30, was characterized by four distinct phases (Bonelli Rubio, 1950; Romero Ortiz, 1951). Initially, the eruption featured moderate phreatomagmatic explosions, ejecting ash, scoria, bombs, and lithics. This was followed by the opening of a 60-m-long fissure, intense faulting, and graben formation, along with a decrease in lava viscosity. Subsequently, a new vent opened, leading to violent phreatomagmatic explosions and substantial ash expulsion. This third phase marked the peak intensity of the eruption. After a brief quiescence, the final phase involved primarily phreatomagmatic activity before the eruption concluded. Petrological studies of the 1949 eruption reveal the involvement of at least three distinct magmas, varying in composition across different vents. These magmas produced basanite, tephrite, and phonotephrite lavas and pyroclasts, some containing abundant xenoliths of crustal and mantle origins (Klügel et al., 2000). The primary melts are believed to have ascended from depths of about 80–100 km. Fractionation of these magmas involved clinopyroxene, olivine, kaersutite and Ti-magnetite at pressures of 600–800 MPa, and possibly 800–1,100 MPa (Klügel et al., 2000). Towards the end of the eruption, xenoliths from the partial collapse of the magmatic plumbing system became common (Klügel et al., 2000). The three magma mixing events that were identified (Klügel et al., 2000) match the timescales of unrest activity (Albert et al., 2016).

The Teneguía eruption in 1971, preceded by felt seismicity several weeks prior to its onset (Albert et al., 2016), was primarily Strombolian and effusive (Afonso et al., 1974; Araña and Fuster, 1974; Araña, 1999), with an estimated volume of erupted material of $4.3 \times 10^{-2}$ km$^3$ (López Acevedo and Pellicer Bautista, 2014). The eruption had two phases. The first phase produced two eruptive centres along a fissure over 300 m long, with abundant lava effusion. The second phase saw the formation of several new vents, but without significant lava effusion, marked instead by intense gas emissions (Afonso et al., 1974; Araña and Fuster, 1974). The composition of the rocks varied between the phases. During the first one, pyroxene basanites with amphibole were emitted while, in the second one, pyroxene-olivine basanites with less amphibole were produced. The MgO content ranged from 6.7 to 7.8 wt. % in the first phase to 8.4–10.2 wt. % in the second phase (Fernández Santín et al., 1974; Ibarrola, 1974). The presence of sodic augite in the lavas suggests differentiation, while clinopyroxene indicates deeper magma storage compared to previous Cumbre Vieja eruptions (Barker et al., 2015). Xenoliths found during the eruption suggest the recycling of earlier magmatic systems (Barker et al., 2015). Magma storage depths during this eruption were comparable to those of the 1949 event. Pre-eruptive timescales calculated from the crystal components have never been calculated.

# 3 The Tajogaite eruption (2021)

The Tajogaite eruption, which occurred in the Cumbre Vieja rift system (Figure 1), began on 19 September 2021, following a period of intense and recurrent geochemical and geophysical anomalies (i.e., seismic swarms and changes in gas emissions) that had been ongoing since 2017 (Torres-González et al., 2020). During the week before the eruption onset the seismic and ground deformation activity strongly increased (Mezcua and Rueda, 2023). The eruptive process lasted for 85 days, ending on 13 December 2021, and involved the emission of primarily lava and tephra with a bulk basanitic composition (Carracedo et al., 2022; Day et al., 2022b). This eruption is the longest-lasting and produced the largest volume of erupted material in La Palma's recorded history over the past 600 years (Carracedo et al., 2022). The eruption had a significant impact, leading to the evacuation of over 8,000 residents, the destruction of almost 3,000 structures (e.g., homes, auxiliary buildings, buildings linked to industry, manufacturing and agriculture, as well as public service facilities), and extensive damage to roads, communication infrastructures, agricultural crops and businesses, and the recurrent closing of the only airport in the island due to volcanic ash falling. All this resulting in economic losses amounted nearly one billion euros (Carracedo et al., 2022; Troll et al., 2024a).

The eruption was preceded by at least 18 seismic swarms since 2017 which can be classified, according to both their depth and their temporal proximity to eruption, as long-term at subcrustal depths prior to 11 September 2021 and short-term at crustal depths after that date (Mezcua and Rueda, 2023). Changes in gas emission were also reported accompanying the seismic series registered during 2017 and 2018 (Torres-González et al., 2020; Benito et al., 2023).

The eruption commenced at 14:12 UTC on 19 September 2021, approximately 20 km northwest of the 1971 eruption site, after high energetic seismic swarms that began on 11 September 2021 (del Fresno et al., 2023; Mezcua and Rueda, 2023). The eruption was primarily Strombolian to Violent Strombolian (following Valentine and Gregg, 2008), characterized by lava fountains and associated flows, explosions, and the emission of ash, lapilli, and lava bombs, although phreatomagmatic episodes were also recorded (Carracedo et al., 2022; Day et al., 2022a).

The formation of the Tajogaite cone began with the emergence of a fissure approximately 1.6 km in length on the northwest flank of Cumbre Vieja. Initially, five vents aligned in a 60°W direction were identified, ranging in elevation between 840 and 1,100 m a.s.l (Romero et al., 2022). During the initial days, explosive activity alternated between lava fountains and Strombolian explosions. Lava primarily flowed towards the western flank. Between September 21 and 24, longer-lasting fountaining episodes, lasting several minutes to hours, became more frequent (Romero et al., 2022). Simultaneously, lava effusion and sporadic Hawaiian fountaining occurred from the north flank vent. The scoria cone rapidly grew to approximately 130 m in height, centred around the main vent (Romero et al., 2022). Several small-scale landslides were observed, but on September 25, a significant lateral collapse affected part of the cone's western flank.

A complete halt in activity, accompanied by a decrease in the tremor signal, lasted approximately 10 h on September 27. Shortly afterward, the explosive activity resumed at the main vent and a shallow seismicity cluster was located between 9 and 13 km depth (del Fresno et al., 2023) remaining active until the end of the eruption. On October 1, a second seismic cluster began between 33 and 38 km depth, lasting until the end of the eruption and showing the highest magnitude events during the eruptive process (del Fresno et al., 2023). At the same time, the fissure architecture became well-defined, with vent activity decoupling (Romero et al., 2022). The upper set of vents in the southernmost part of the fissure mainly produced explosive activity, exhibiting Strombolian activity and intermittent lava fountaining, generating ash columns varying in height. The lowermost northwestern vents were responsible for effusive activity and Hawaiian fountaining.

The final phase of the eruption took place on December 13. A significant explosion produced the highest eruptive column during the whole eruption that reached a height of 8.5 km a.s.l. (Carracedo et al., 2022).

# 4 Methodology and monitoring network

## 4.1 Eruption sampling

Two sets of samples carefully collected during the Tajogaite eruption have been considered for this study. In both cases, sampling was systematically performed during the eruption, allowing for the collection of material that was frequently covered by subsequent emissions. The emission date of all samples is known (Table 1).

The first set, consisting of 42 samples, comprises ash, lapilli, and lava flows, and was collected by the IGN Volcano Monitoring Team (Instituto Geográfico Nacional, Spain). Ash and lapilli samples were recovered by placing clean plastic/paper films or containers over flat surfaces directly under the dispersion field of the eruptive column. Lava flows were sampled while they were still incandescent or hot, quenching the samples with water until they were cool enough to be handled. In cases where lava flows could not be sampled while incandescent, they were collected as soon as possible after their emission. From this set, 17 samples covering the whole eruption period were analysed for major and trace elements, including the first and last emitted materials.

The second set comprises seven samples selected from the full collection of lava samples included in Day et al. (2022b). These samples were obtained through systematic sampling carried out throughout the entire eruption period and were prepared and archived by the University of Las Palmas de Gran Canaria and the University of Barcelona. From this collection, we selected seven samples spaced in time throughout the eruption, including the first and last emitted materials. These samples were considered for petrographic description, electron microprobe analyses and diffusion chronometry models. To select the samples, we considered not only their temporal distribution throughout the eruption, but also their proximity to notable seismic events, periods of seismic calm, or shifts in the earthquake foci. Samples LP21-02 and LP21-04 were chosen from a lava batch emitted shortly after the eruption commenced on September 20 and 21. Samples LP21-65 (October 27) and LP21-77 (November 15) were collected following a peak in the number of earthquakes and after a period of quiescence, respectively. Sample LP21-91 (November 28) was collected during a period of quiescence following several seismic swarms and a shift in the earthquakes to a shallower level. Samples LP21-90 and LP21-94 correspond to the final materials expelled from the eruption, comprising a lava sample and a porphyritic Strombolian bomb, respectively.

## 4.2 Petrography and geochemistry

Seventeen samples (lava, lapilli, and ash) from the IGN (Instituto Geográfico Nacional) set were sent to the Instituto Andaluz de Ciencias de la Tierra (UGR-CSIC; Spain) for whole-rock geochemical analysis of major elements by X-Ray Fluorescence (XRF) using a WDXRF S4 Pioneer BRUKER equipment, after crushing, mill-grinding with a tungsten ball-mill, mixing with lithium tetraborate for melting at 1,000 °C and re-solidifying the material in vitreous beads by quenching. Loss On Ignition (LOI) was also measured and found to be negligible (16 samples with LOI < 0.08%, one sample with LOI = 0.79%; see Table 1). Instrumental precision for major elements was 0.3% (0.5% for $Na_2O$). Trace elements were analysed by Inductively Coupled Plasma Mass Spectrometry (ICP-MS) at the Centro de Instrumentación Científica of the Universidad de Granada (UGR) using a NexION 300D instrument, with a precision of 2% at 50 ppm concentration.

Petrography was conducted on thin sections from the 17 samples analysed in Day et al. (2022b) with an optical petrographic microscope to determine the main textural characteristics of the studied deposits. A detailed compositional study of the olivine crystals was conducted at the Scientific and Technological Centers of the University of Barcelona using a JEOL JXA 8230 Electron

TABLE 1 Major and trace elements analyses results.

| Sample: IGN- | 3a | 3b | 9 | 11 | 28 | 14 | 22 | 26 | 29 | 30 | 34 | 36 | 38 | 40 | 37 | 41 | 42 |
|---|---|---|---|---|---|---|---|---|---|---|---|---|---|---|---|---|---|
| Deposit type | Lava flow | Lava flow | Lava flow | Lapilli | Ash | Lava flow | Lava flow | Ash | Ash | Ash | Ash | Lava flow | Lava flow | Lava flow | Lapilli | Lava flow | Ash |
| Emission date | 22 September 2021 | 22 September 2021 | 30 September 2021 | 01 October 2021 | 05 October 2021 | 09 October 2021 | 20 October 2021 | 03 November 11/2021 | 09 November 2021 | 15 November 2021 | 22 November 2021 | 22 November 2021 | 25 November 2021 | 25 November 2021 | 25 November 2021 | 05 December 12/2021 | 13 December 2021 |
| $SiO_2$ | 43.87 | 43.92 | 43.59 | 43.49 | 45.47 | 43.62 | 43.8 | 43.49 | 43.54 | 43.79 | 43.59 | 43.38 | 42.83 | 43.34 | 44.85 | 44.2 | 44.24 |
| $TiO_2$ | 3.79 | 3.73 | 3.6 | 3.54 | 3.55 | 3.5 | 3.5 | 3.58 | 3.6 | 3.68 | 3.58 | 3.6 | 3.54 | 3.55 | 3.55 | 3.57 | 3.61 |
| $Al_2O_3$ | 14.57 | 14.39 | 13.86 | 13.48 | 13.85 | 13.32 | 12.96 | 13.55 | 13.51 | 13.75 | 13.19 | 13.24 | 12.9 | 13.01 | 12.76 | 13.31 | 13.85 |
| $Fe_2O_3$ | 13.38 | 13.24 | 13.49 | 13.4 | 13.15 | 13.9 | 13.45 | 13.71 | 13.54 | 13.76 | 13.71 | 13.66 | 13.44 | 13.64 | 13.53 | 13.39 | 13.27 |
| MnO | 0.2 | 0.2 | 0.2 | 0.19 | 0.19 | 0.19 | 0.19 | 0.19 | 0.19 | 0.19 | 0.19 | 0.19 | 0.19 | 0.19 | 0.18 | 0.19 | 0.19 |
| MgO | 5.9 | 6.06 | 7.48 | 8.08 | 7.28 | 8.27 | 8.45 | 7.68 | 7.85 | 7.54 | 8.48 | 8.12 | 8.3 | 8.56 | 8.5 | 7.83 | 6.81 |
| CaO | 10.25 | 10.64 | 10.71 | 10.86 | 10.46 | 10.93 | 11.67 | 11.12 | 11.16 | 11.47 | 11.61 | 11.65 | 11.6 | 11.59 | 11.65 | 11.52 | 11.02 |
| $Na_2O$ | 4.23 | 4.2 | 3.98 | 3.81 | 4.1 | 3.83 | 3.57 | 3.68 | 3.68 | 3.75 | 3.59 | 3.59 | 3.49 | 3.49 | 3.47 | 3.77 | 3.97 |
| $K_2O$ | 1.78 | 1.7 | 1.68 | 1.59 | 1.67 | 1.52 | 1.38 | 1.5 | 1.53 | 1.49 | 1.39 | 1.4 | 1.33 | 1.37 | 1.32 | 1.48 | 1.61 |
| $P_2O_5$ | 1.05 | 1.02 | 0.84 | 0.81 | 0.84 | 0.78 | 0.68 | 0.77 | 0.79 | 0.8 | 0.79 | 0.78 | 0.77 | 0.78 | 0.78 | 0.81 | 0.85 |
| LOI(%) | 0.06 | 0.08 | 0 | 0.02 | 0 | 0 | 0 | 0 | 0 | 0 | 0 | 0 | 0.79 | 0 | 0 | 0 | 0 |
| Zr | 344 | 336 | 314 | 304 | 317 | 289 | 268 | 279 | 274 | 267 | 260 | 266 | 263 | 260 | 261 | 279 | 287 |
| Sr | 1,249 | 1,212 | 1,104 | 1,060 | 1,110 | 1,020 | 926 | 1,007 | 1,018 | 1,022 | 994 | 1,000 | 1,000 | 1,000 | 1,003 | 1,063 | 1,119 |
| Cr | 224 | 206 | 387 | 364 | 372 | 816 | 483 | 429 | 452 | 409 | 478 | 506 | 461 | 421 | 438 | 412 | 226 |
| Ni | 53 | 61 | 108 | 120 | 101 | 137 | 136 | 108 | 120 | 108 | 133 | 125 | 132 | 139 | 135 | 116 | 97 |
| Li | 9.99 | 10.02 | 8.99 | 8.63 | 7.85 | 7.67 | 5.86 | 7.21 | 7.05 | 6.71 | 6.47 | 6.52 | 6.33 | 6.60 | 6.29 | 6.92 | 7.00 |
| Rb | 37.05 | 37.53 | 37.58 | 34.96 | 35.14 | 32.23 | 30.24 | 31.98 | 32.39 | 31.27 | 29.58 | 29.27 | 27.13 | 28.92 | 25.76 | 29.02 | 30.01 |
| Cs | 0.39 | 0.39 | 0.45 | 0.43 | 0.43 | 0.41 | 0.36 | 0.45 | 0.40 | 0.40 | 0.38 | 0.38 | 0.35 | 0.37 | 0.33 | 0.36 | 0.37 |
| Be | 2.68 | 2.62 | 2.08 | 2.13 | 2.23 | 2.02 | 1.84 | 1.89 | 1.93 | 2.00 | 1.89 | 1.95 | 1.88 | 1.95 | 1.80 | 2.01 | 2.00 |
| Sr | 1,149.23 | 1,152.99 | 1,087.10 | 1,043.59 | 1,039.49 | 972.65 | 903.45 | 989.90 | 1,029.45 | 1,009.84 | 986.77 | 965.82 | 932.83 | 978.17 | 906.13 | 989.73 | 1,003.79 |
| Ba | 630.35 | 630.67 | 573.84 | 548.15 | 514.29 | 493.41 | 444.52 | 490.28 | 493.95 | 464.60 | 449.03 | 443.33 | 422.93 | 439.71 | 412.13 | 454.25 | 460.63 |
| Sc | 25.82 | 25.57 | 23.95 | 24.54 | 24.68 | 24.08 | 30.23 | 26.31 | 27.42 | 27.22 | 28.11 | 29.32 | 28.30 | 29.22 | 28.09 | 28.42 | 22.18 |
| V | 344.33 | 343.64 | 309.80 | 305.38 | 291.08 | 317.37 | 331.70 | 325.30 | 333.36 | 347.95 | 348.57 | 349.16 | 332.31 | 350.20 | 302.45 | 308.13 | 291.04 |
| Cr | 227.77 | 225.95 | 358.08 | 331.05 | 327.75 | 833.79 | 449.22 | 431.34 | 460.68 | 395.88 | 481.25 | 505.06 | 414.87 | 415.09 | 379.29 | 347.09 | 176.11 |
| Co | 43.53 | 42.70 | 46.36 | 47.66 | 43.39 | 49.03 | 49.18 | 47.39 | 48.99 | 47.87 | 51.63 | 49.69 | 48.88 | 51.94 | 47.30 | 46.21 | 41.36 |

(Continued on the following page)

TABLE 1 (*Continued*) Major and trace elements analyses results.

| Sample: IGN- | 3a | 3b | 9 | 11 | 28 | 14 | 22 | 26 | 29 | 30 | 34 | 36 | 38 | 40 | 37 | 41 | 42 |
|---|---|---|---|---|---|---|---|---|---|---|---|---|---|---|---|---|---|
| Deposit type | Lava flow | Lava flow | Lava flow | Lapilli | Ash | Lava flow | Lava flow | Ash | Ash | Ash | Ash | Lava flow | Lava flow | Lava flow | Lapilli | Lava flow | Ash |
| Emission date | 22 September 2021 | 22 September 2021 | 30 September 2021 | 01 October 2021 | 05 October 2021 | 09 October 2021 | 20 October 2021 | 03 November 11/2021 | 09 November 2021 | 15 November 2021 | 22 November 2021 | 22 November 2021 | 25 November 2021 | 25 November 2021 | 25 November 2021 | 05 December 12/2021 | 13 December 2021 |
| Ni | 56.51 | 55.99 | 106.22 | 117.06 | 102.53 | 150.40 | 141.31 | 125.17 | 133.68 | 116.09 | 148.02 | 129.12 | 133.24 | 137.32 | 131.11 | 121.74 | 94.40 |
| Cu | 79.59 | 79.73 | 96.52 | 91.78 | 67.96 | 97.85 | 102.63 | 101.27 | 106.22 | 110.18 | 108.44 | 106.17 | 104.91 | 108.07 | 80.33 | 80.55 | 85.20 |
| Zn | 141.61 | 140.09 | 137.38 | 131.68 | 117.60 | 125.19 | 121.99 | 127.66 | 127.74 | 127.56 | 124.55 | 123.85 | 128.01 | 127.52 | 115.89 | 118.11 | 124.67 |
| Ga | 25.02 | 24.86 | 23.04 | 22.48 | 23.14 | 21.56 | 21.68 | 22.09 | 22.50 | 22.69 | 22.10 | 21.11 | 20.30 | 21.60 | 20.99 | 22.34 | 22.01 |
| Y | 35.42 | 36.05 | 33.00 | 31.65 | 31.50 | 30.06 | 29.09 | 30.48 | 31.31 | 30.76 | 30.50 | 29.95 | 29.15 | 30.27 | 28.46 | 30.33 | 29.90 |
| Nb | 90.33 | 90.44 | 77.10 | 73.49 | 74.91 | 70.87 | 63.88 | 68.14 | 68.45 | 66.70 | 64.86 | 64.15 | 59.89 | 63.64 | 61.56 | 68.00 | 67.77 |
| Ta | 5.28 | 5.00 | 5.04 | 4.76 | 5.07 | 4.59 | 4.16 | 4.42 | 4.42 | 4.26 | 4.20 | 4.35 | 3.84 | 4.03 | 4.16 | 4.43 | 4.50 |
| Zr | 356.52 | 355.71 | 315.85 | 304.47 | 339.66 | 286.22 | 268.83 | 273.51 | 273.46 | 267.55 | 261.05 | 260.05 | 245.93 | 261.43 | 244.64 | 297.69 | 295.95 |
| Hf | 8.26 | 8.21 | 7.36 | 6.83 | 6.87 | 6.31 | 6.02 | 5.97 | 5.99 | 6.21 | 6.13 | 6.08 | 5.83 | 6.09 | 5.84 | 6.06 | 5.93 |
| Mo | 8.89 | 8.85 | 9.36 | 7.40 | 7.13 | 20.41 | 7.76 | 8.23 | 7.96 | 6.65 | 7.04 | 8.12 | 6.29 | 6.09 | 6.09 | 7.42 | 4.10 |
| Sn | 2.90 | 2.87 | 2.12 | 1.92 | 1.62 | 0.77 | 0.46 | 0.99 | 0.63 | 1.62 | 0.84 | 2.27 | 1.84 | 2.08 | 1.49 | 1.77 | 1.98 |
| Tl | 0.04 | 0.03 | 0.06 | 0.05 | 0.10 | 0.06 | 0.05 | 0.09 | 0.09 | 0.10 | 0.07 | 0.05 | 0.05 | 0.05 | 0.05 | 0.04 | 0.09 |
| Pb | 4.08 | 4.39 | 3.69 | 2.97 | 3.37 | 3.36 | 3.11 | 3.77 | 3.46 | 3.54 | 3.02 | 2.96 | 2.92 | 2.96 | 2.45 | 2.85 | 3.85 |
| U | 2.56 | 2.45 | 2.20 | 2.07 | 2.22 | 1.93 | 1.78 | 1.91 | 1.90 | 1.88 | 1.82 | 1.82 | 2.16 | 1.81 | 1.73 | 1.94 | 1.97 |
| Th | 8.09 | 8.04 | 8.02 | 7.27 | 7.69 | 6.78 | 6.11 | 6.74 | 6.80 | 6.94 | 6.51 | 6.49 | 6.15 | 6.48 | 6.18 | 7.17 | 7.00 |
| La | 97.42 | 97.22 | 84.17 | 80.45 | 75.80 | 72.20 | 66.39 | 71.91 | 73.90 | 67.76 | 67.04 | 65.99 | 63.54 | 66.67 | 64.41 | 71.07 | 71.40 |
| Ce | 188.42 | 189.54 | 160.10 | 154.54 | 148.10 | 140.87 | 127.52 | 138.73 | 141.72 | 131.23 | 129.53 | 128.52 | 124.45 | 130.61 | 124.41 | 139.47 | 140.34 |
| Pr | 22.03 | 22.11 | 18.35 | 17.76 | 16.68 | 16.30 | 14.97 | 16.12 | 16.57 | 15.35 | 15.25 | 15.04 | 14.66 | 15.23 | 14.74 | 16.03 | 15.97 |
| Nd | 87.93 | 88.11 | 69.38 | 67.56 | 64.27 | 62.73 | 58.06 | 62.62 | 64.19 | 59.84 | 59.25 | 58.84 | 57.31 | 59.56 | 57.67 | 61.41 | 61.86 |
| Sm | 15.96 | 16.22 | 12.89 | 12.24 | 11.86 | 11.69 | 11.12 | 11.64 | 11.97 | 11.31 | 11.35 | 11.08 | 10.73 | 11.32 | 10.83 | 11.57 | 11.50 |
| Eu | 4.47 | 4.60 | 4.11 | 4.02 | 3.93 | 3.77 | 3.64 | 3.84 | 3.95 | 3.80 | 3.83 | 3.46 | 3.39 | 3.53 | 3.67 | 3.89 | 3.79 |
| Gd | 11.61 | 11.96 | 9.36 | 9.05 | 8.81 | 8.26 | 7.89 | 8.31 | 8.57 | 8.14 | 8.36 | 8.43 | 8.18 | 8.50 | 8.02 | 8.60 | 8.32 |
| Tb | 1.63 | 1.68 | 1.22 | 1.17 | 1.13 | 1.08 | 1.04 | 1.10 | 1.12 | 1.08 | 1.08 | 1.18 | 1.14 | 1.19 | 1.07 | 1.11 | 1.09 |
| Dy | 8.64 | 8.90 | 6.29 | 6.08 | 5.74 | 5.49 | 5.32 | 5.56 | 5.68 | 5.54 | 5.52 | 6.27 | 6.10 | 6.29 | 5.33 | 5.64 | 5.54 |
| Ho | 1.54 | 1.61 | 1.08 | 1.04 | 1.02 | 0.98 | 0.95 | 0.99 | 1.02 | 1.00 | 0.99 | 1.09 | 1.05 | 1.10 | 0.94 | 1.00 | 0.98 |

(Continued on the following page)

TABLE 1 *(Continued)* Major and trace elements analyses results.

| Sample: IGN- | 3a | 3b | 9 | 11 | 28 | 14 | 22 | 26 | 29 | 30 | 34 | 36 | 38 | 40 | 37 | 41 | 42 |
|---|---|---|---|---|---|---|---|---|---|---|---|---|---|---|---|---|---|
| Deposit type | Lava flow | Lava flow | Lava flow | Lapilli | Ash | Lava flow | Lava flow | Ash | Ash | Ash | Ash | Lava flow | Lava flow | Lava flow | Lapilli | Lava flow | Ash |
| Emission date | 22 September 2021 | 22 September 2021 | 30 September 2021 | 01 October 2021 | 05 October 2021 | 09 October 2021 | 20 October 2021 | 03 November 11/2021 | 09 November 2021 | 15 November 2021 | 22 November 2021 | 22 November 2021 | 25 November 2021 | 25 November 2021 | 25 November 2021 | 05 December 12/2021 | 13 December 2021 |
| Er | 3.52 | 3.68 | 2.38 | 2.29 | 2.29 | 2.18 | 2.12 | 2.19 | 2.23 | 2.21 | 2.20 | 2.68 | 2.57 | 2.69 | 2.12 | 2.22 | 2.19 |
| Tm | 0.45 | 0.46 | 0.31 | 0.30 | 0.30 | 0.29 | 0.28 | 0.29 | 0.29 | 0.29 | 0.29 | 0.36 | 0.34 | 0.36 | 0.28 | 0.29 | 0.29 |
| Yb | 2.61 | 2.69 | 1.74 | 1.72 | 1.71 | 1.60 | 1.54 | 1.60 | 1.65 | 1.62 | 1.62 | 2.02 | 1.95 | 2.03 | 1.56 | 1.63 | 1.63 |
| Lu | 0.39 | 0.40 | 0.25 | 0.25 | 0.25 | 0.23 | 0.23 | 0.23 | 0.24 | 0.24 | 0.23 | 0.30 | 0.28 | 0.29 | 0.23 | 0.24 | 0.24 |

Probe Microanalyser (EPMA) with acceleration voltage of 20 kV and 20 nA beam current, calibrated with reference minerals. In total we analysed 27 olivine crystals appertaining to the seven selected samples described in the previous section. Additionally, we performed compositional profiles in 14 olivine crystals from six samples (punctual analyses every 2 µm). Data can be found as Supplementary Material (Supplementary Table S1).

Electron backscattered diffraction (EBSD) patterns of olivine were obtained at the Department of Materials Science and Engineering of the Universitat Politècnica de Catalunya (UPC) using a JEOL JSM-7001F equipped with an Oxford/HKL detector and HKL CHANNEL5 software. In total, 10 determinations were successful, as the EBSD method works only when surface conditions are optimal.

### 4.2.1 Diffusion chronometry

We modelled the Fe-Mg, Ni and Mn concentration gradients using the program DIPRA (Girona and Costa, 2013) including the effects of diffusion anisotropy by processing the EBSD data. We report the uncertainty on diffusion times that accounts for analytical and temperature uncertainty as calculated by DIPRA. In addition, DIPRA also calculates a parameter called "discrepancy", which represents a goodness of the fit (Girona and Costa, 2013) and which is reported in Table 2. All the Fe-Mg and Ni diffusion times were obtained from fits with a discrepancy of ≤10%, except for one (LP21-90-2; 15%). Because of the analytical resolution of the data, we were not able to achieve this standard for the Mn models. These models were fitted with a discrepancy value under 18%. The temperature, pressure, and oxygen fugacity ($fO_2$) buffer used for modelling are 1,170 °C ± 10 °C, 3 kbar (upper magma stagnation level), and QFM+1, respectively, based on previous publications (Klügel et al., 2005; Castro and Feisel, 2022; D'Auria et al., 2022; Day et al., 2022b; Romero et al., 2022; Burton et al., 2023; Dayton et al., 2023; Fabbrizio et al., 2023; González-García et al., 2023; Sandoval-Velasquez et al., 2023; Ubide et al., 2023; Bonechi et al., 2024; Zanon et al., 2024). Reasonable variations in pressure and oxygen fugacity for this geological context are expected to have a secondary effect relative to the temperature uncertainty.

## 4.3 Dissolved gasses

Since the beginning of 2016, the IGN has been sampling groundwater from a tide-pool (QP63) located 5 km southwest from the Tajogaite eruption vents (Figure 2). Total composition of dissolved gases has been analysed. In this work, He and $CO_2$ concentrations in groundwater dissolved gas are reported.

Gas samples were obtained every two-three months, using the method described in Capasso and Inguaggiato (1998). The analyses were carried out at INGV laboratories at Palermo (Italy) following the methodology described in Paonita et al. (2012).

## 4.4 GNSS

In September 2021, the GNSS (Global Navigation Satellite System) monitoring network deployed at La Palma Island was

TABLE 2 Timescales (in days) calculated by modelling the chemical diffusion of Fe–Mg (Fo), Ni, and Mn in olivine crystals.

| Emission date | Sample | Crystal | Element | P1 | P2 | B | α | β | γ | Time | Δ(−) | Δ(+) | Discr. (%) | Calculated date |
|---|---|---|---|---|---|---|---|---|---|---|---|---|---|---|
| 27 October 2021 | LP-21-65 | 4 | Fo | 0.819 | 0.833 | 0.815 | 78.9 | 149.3 | 108.8 | 43 | 6 | 9 | 9 | 13 September 2021 |
| | | | Ni | 0.177 | 0.213 | 0.170 | 78.9 | 149.3 | 108.8 | 49 | 8 | 11 | 9 | 07 September 2021 |
| | | 6 | Fo | 0.807 | 0.829 | 0.816 | 106.5 | 134.4 | 66.6 | 40 | 5 | 5 | 9 | 16 September 2021 |
| | | | Ni | 0.176 | 0.199 | 0.172 | 106.5 | 134.4 | 66.6 | 48 | 8 | 10 | 3 | 08 September 2021 |
| | | | Mn | 0.270 | 0.249 | 0.293 | 106.5 | 134.4 | 66.6 | 43 | 6 | 6 | 13 | 13 September 2021 |
| 15 November 2021 | LP-21-77 | 3 | Fo | 0.840 | 0.831 | 0.789 | 53.1 | 128 | 96.2 | 55 | 6 | 9 | 2 | 20 September 2021 |
| | | | Ni | 0.255 | 0.190 | 0.121 | 53.1 | 128 | 96.2 | 80 | 21 | 13 | 4 | 27 August 2021 |
| | | | Mn | 0.221 | 0.250 | 0.329 | 53.1 | 128 | 96.2 | 57 | 7 | 9 | 14 | 18 September 2021 |
| | | 10 | Fo | 0.817 | 0.830 | 0.807 | 45.3 | 115.1 | 85.4 | 81 | 18 | 17 | 4 | 26 August 2021 |
| | | | Ni | 0.175 | 0.194 | 0.140 | 45.3 | 115.1 | 85.4 | 127 | 30 | 19 | 4 | 11 July 2021 |
| | | | Mn | 0.259 | 0.245 | 0.320 | 45.3 | 115.1 | 85.4 | 64 | 8 | 11 | 13 | 11 September 2021 |
| 28 November 2021 | LP-21-91 | 5 | Fo | 0.807 | 0.830 | 0.814 | 110.2 | 46.4 | 63.3 | 44 | 5 | 6 | 2 | 15 October 2021 |
| | | | Ni | 0.165 | 0.185 | 0.153 | 110.2 | 46.4 | 63.3 | 46 | 10 | 8 | 4 | 13 October 2021 |
| | | | Mn | 0.276 | 0.251 | 0.291 | 110.2 | 46.4 | 63.3 | 47 | 5 | 6 | 10 | 11 October 2021 |
| | | 7 | Fo | 0.829 | 0.834 | 0.810 | 74.2 | 144.5 | 104.6 | 48 | 8 | 9 | 0 | 10 October 2021 |
| | | | Ni | 0.187 | 0.200 | 0.154 | 74.2 | 144.5 | 104.6 | 48 | 19 | 29 | 0 | 11 October 2021 |
| 10 December 2021 | LP-21-90 | 5 | Fo | 0.835 | | 0.819 | 58.5 | 129.6 | 93.2 | 32 | 15 | 15 | 4 | 08 November 2021 |
| | | | Ni | 0.195 | | 0.147 | 58.5 | 129.6 | 93.2 | 23 | 9 | 22 | 2 | 17 November 2021 |
| | | | Mn | 0.240 | | 0.294 | 58.5 | 129.6 | 93.2 | 44 | 6 | 12 | 6 | 27 October 2021 |
| | | 1 | Fo | 0.836 | | 0.791 | 102.2 | 24.9 | 89.9 | 23 | 4 | 3 | 5 | 16 November 2021 |
| | | | Ni | 0.186 | | 0.119 | 102.2 | 24.9 | 89.9 | 17 | 7 | 5 | 10 | 22 November 2021 |
| | | | Mn | 0.230 | | 0.307 | 102.2 | 24.9 | 89.9 | 49 | 14 | 12 | 18 | 22 October 2021 |

(Continued on the following page)

TABLE 2 (*Continued*) Timescales (in days) calculated by modelling the chemical diffusion of Fe–Mg (Fo), Ni, and Mn in olivine crystals.

| Emission date | Sample | Crystal | Element | P1 | P2 | B | α | β | γ | Time | Δ(−) | Δ(+) | Discr. (%) | Calculated date |
|---|---|---|---|---|---|---|---|---|---|---|---|---|---|---|
| | | 3 | Fo | 0.816 | 0.831 | 0.790 | 104.4 | 29.4 | 83.9 | 43 | 7 | 11 | 4 | 27 October 2021 |
| | | | Ni | 0.157 | 0.182 | 0.132 | 104.4 | 29.4 | 83.9 | 48 | 26 | 9 | 4 | 22 October 2021 |
| | | | Mn | 0.257 | 0.235 | 0.315 | 104.4 | 29.4 | 83.9 | 73 | 10 | 15 | 14 | 27 September 2021 |
| | | 2 | Fo | 0.802 | 0.842 | 0.831 | 45.9 | 117 | 87.9 | 762 | 88 | 104 | 15 | 09 November 2019 |

P1 and P2 are the two compositional plateaus observed leading to reverse zoning. B is the boundary composition. We report the angles between the traverses and the three crystallographic axis (α, β, γ) and the discrepancy value (in percentage). The analytical errors are ±0.2 for the Fo (mol%) and ±0.015 for the NiO and MnO (wt%). Δ(−) and Δ(+) are the errors on the total time calculated by DIPRA, after the anisotropy correction based on the EBSD data. The temperatures and $fO_2$ values are indicated in the main text.

composed by the dual frequency receivers LPAL, LP01, LP02, LP03, LP04, LP05, LP06 and MAZO, which are represented in Figure 2. Real-time communication allows the RINEX data acquisition. All these GNSS permanent stations are IGN owned, except the Canarian Regional Government publicly available MAZO (GRAFCAN, 2019).

The RINEX observation data were processed as described in Lamolda et al. (2017) for the case of El Hierro Island. We obtained subdaily (30 s sampling) coordinate solutions in ITRF2014 reference frame (Altamimi et al., 2016). Finally, we used a Kalman filtering strategy to enhance the subdaily position estimates. In this case, for La Palma GNSS network, as reference stations we have opted for the permanent stations of IZAN (Tenerife Island) and MAS1 (Gran Canaria Island), as both have a long time series dataset.

## 4.5 InSAR

Surface deformation has also been measured using InSAR data. A dataset of 101 Sentinel-1 images (SLC IW) from the relative orbit numbered 60 was used. This dataset covers the period from 16 May 2020 to 05 February 2022 and it was processed using GAMMA software and applying the multi-temporal methodology called Small Baseline Subset (SBAS; Wegmüller et al., 2004).

Multi-temporal (MT) techniques can help to mitigate the disturbances which affect differential interferograms caused by atmospheric effects and spatio-temporal decorrelation noise. SBAS approach uses a large number of small perpendicular and temporal baselines interferograms as a way to overcome the differential interferometry (DInSAR) limiting factors (Ferretti et al., 2001; Berardino et al., 2002; Hooper et al., 2012). As a result, we obtain time series of deformation between May 2020 and February 2022 for selected pixels in the images. These time series are calculated in the Line Of Sight of the satellite (LOS) as this is the direction of the measurement signal (Hanssen, 2001).

In this case, we considered multi-looked differential interferometric phases using 11 range and 3 azimuth looks and a maximum baseline of 250 m. In order to include redundant observations, we use each scene 5 times as the master scene with the result that a maximum temporal baseline for the scene pairs used is 54 days. According to these conditions, the total number of interferograms used for the time series generation is 487. We have not applied any further advanced refinement to the time series in order to allow the detection of any sudden deformation caused by magma displacement and to preclude it to be distributed over time. We selected a reference point centred in the scene, showing good coherence and a quite stable behaviour (Figure 2D). To remove the topographic phase from the interferograms, a high-resolution derived model from MDT05 5-m was used (Civico et al., 2022).

## 4.6 Real-time visual monitoring of the eruptive column height

IGN, as part of its official duties monitoring the volcanic activity, performed the quantitative description of the volcanic eruptive column, required for PEVOLCA (Special Plan for Civil Protection and Emergency Response to Volcanic Risk in the Canary Islands) Committees during the crisis. These results were also included in

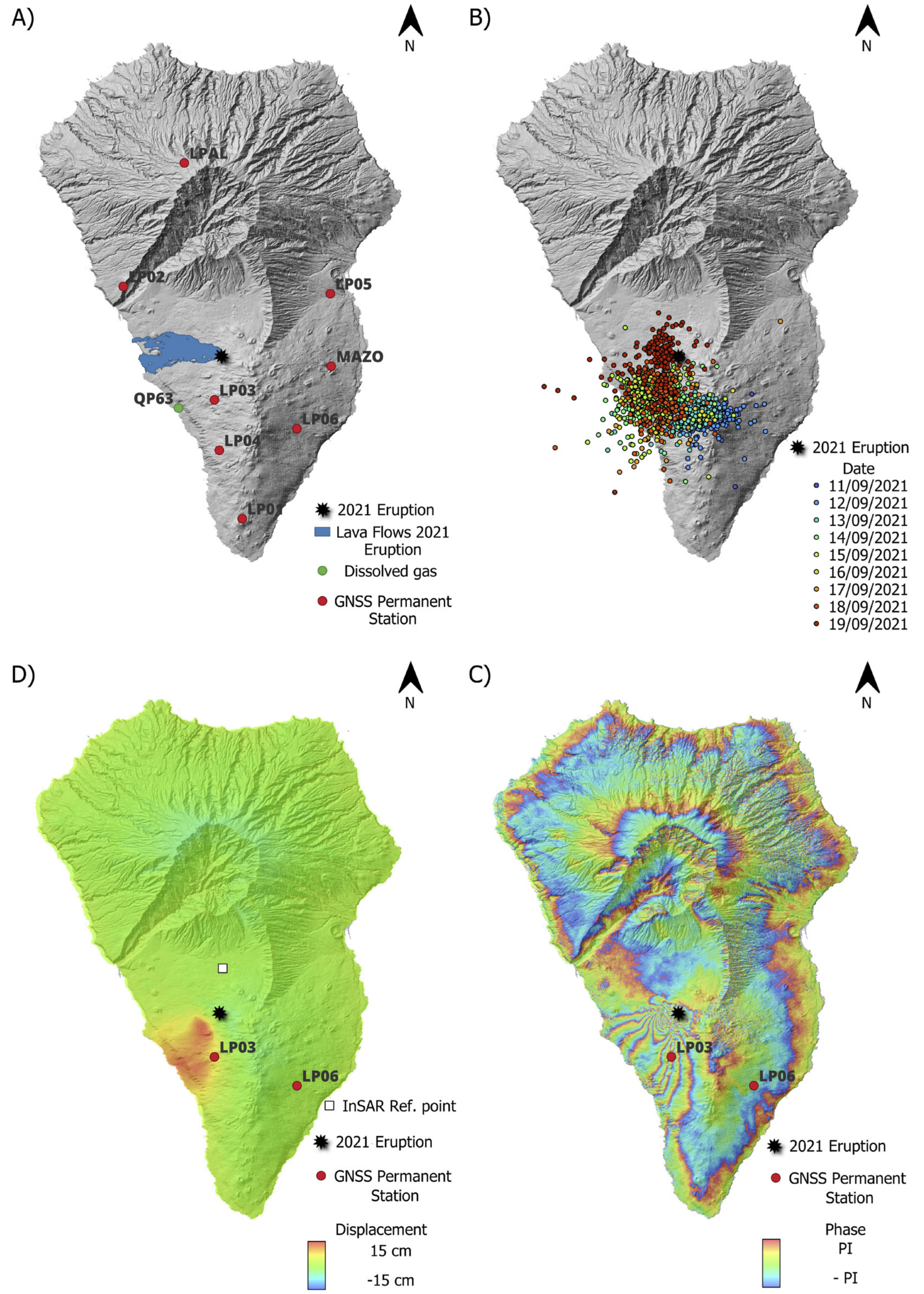

FIGURE 2
**(A)** Distribution of GNSS permanent stations and dissolved gas and water sampling point. The 2021 lava flows are marked in blue. **(B)** Seismicity located on La Palma during the 9 days of unrest preceding the eruption. A migration of the seismicity from E to W, and later to N can be observed (colours represent time-evolution). **(C)** Sentinel 1 wrapped interferogram between 8 and 20 September 2021. **(D)** LOS Ground displacements derived from **(C)**.

the VONA (Volcano Observatory Notice for Aviation) emissions and in the regular reports to Toulouse VAAC (Volcanic Ash Advisory Centre) (Felpeto et al., 2022).

The eruptive column-height monitoring network consisted of three calibrated webcams providing scaled images of the eruptive column at real time. A webcam of E.U. EELabs project, coordinated by the Instituto de Astrofísica de Canarias (IAC), located at the Roque de Los Muchachos facilities, 16 km to the north of the eruptive process and installed prior to the eruption, was used as the reference webcam. Its north-south orientation was perpendicular to the predominant winds and its altitude and distance from the volcano avoided inclination of the images, therefore the camera allowed a proper estimation of the column height and its morphological variations. In addition, two other cameras were installed at different locations by IGN, to have secondary measures from other perspectives, and thus to obtain a better understanding of the influence of the winds.

The scale of each image was calculated by knowing the camera's internal optical parameters and its distance from the vent. Then, a scaled grid was automatically superimposed on the images, providing immediate measures. On this grid we included the wind direction and speed at different heights provided by AEMET (Agencia Estatal de Meteorología), which are useful for the correct estimation of the column height. To check and calibrate the scale obtained, geodetic techniques (trigonometric levelling) were applied (Kähmen and Faig, 1988). Different altitudes (in m.a.s.l.) were measured along the eruptive column simultaneously with a theodolite and on the scaled images.

# 5 Results

## 5.1 Petrographic description of the erupted lava

The volcanic products emitted during the 2021 La Palma eruption and studied in this work exhibit a range from massive to highly vesicular textures, with vesicle contents reaching up to 40%–50%. The samples display porphyritic textures and a typical mineral assemblage consisting of clinopyroxene, olivine, Fe-Ti oxides, and occasionally amphibole phenocrysts (Figure 3), the latter primarily observed in the earliest lavas (i.e., the first 20 days of the eruption; samples LP21-02 and 04) and in the volcanic bomb from the last days of the eruption (LP21-94). Plagioclase is restricted to microlites within a glassy to fine-grained groundmass, accompanied by microcrysts of clinopyroxene, olivine, and Fe-Ti oxides. Phenocrysts mostly occur as individual subhedral crystals, but crystal clots and glomerophyric aggregates are also common (Figure 3C).

Clinopyroxene is the main mineral phase in the 2021 La Palma products, with multiple clinopyroxene populations consistently present in all volcanic products, reaching up to 20 vol.% and sizes ranging from 5 to 6 mm. The presence of multiple populations is indicated by complex crystal textures, including zoning and disequilibrium features such as sieve textures. Phenocrysts range from colourless or light brown to green, with subhedral to anhedral core shapes.

Olivine primarily occurs as subhedral complex zoned crystals with sizes up to 1 mm and abundances ranging from 6 to 8 vol.% in all the studied 2021 La Palma products. However, in the lavas emitted during the first week of the eruption (samples LP21-02 and 04), olivine content is scarce (less than 1 to 2 vol%), with some exhibiting skeletal crystal growth. The olivine content and size increased as the eruption progressed. In some samples, anhedral olivine cores are mantled by Fe-Ti oxides intergrown with clinopyroxene crystals (LP21-65, 77, 90 and 91).

Amphibole is present only in the lavas erupted during the first 2 weeks (LP21-02 and 04) and in the final explosive event on 13 December 2021 (sample LP21-94). Subhedral to anhedral amphibol crystals, up to 6 mm in size and comprising less than 2–5 vol%, show typical disequilibrium textures with Fe-Ti oxide reaction rims suggesting destabilization of amphiboles during magma ascent towards the surface (e.g., Fabbrizio et al., 2023).

Fe-Ti oxides occur as euhedral to subhedral phenocrysts and microlites in all lavas. While some are isolated, Fe-Ti oxide glomerocrysts are abundant. They also appear as minute inclusions in olivine and clinopyroxene crystals or as a mineral phase in some of the cumulate fragments spanning the entire volcanic eruption.

## 5.2 Geochemical evolution of the erupted material

Bulk rock major and trace element contents are reported for 17 new volcanic products (lava $N = 9$, ash $N = 6$, and lapilli $N = 2$) spanning the 85 days of the 2021 Tajogaite eruption (Table 1), along with the data reported in Day et al. (2022b) for comparison. The analysed samples fall within the tephrite/basanite field of the TAS diagram (le Maitre et al., 1989) and exhibit a transition towards more mafic compositions from the beginning of the eruption. MgO contents range from up to 6.1 wt% in lavas emitted during the first days of the eruption (tephrites represented by samples IGN-3a and 3b) to 8.6 wt% in lavas emitted at the end of November 2021 (basanite sample IGN-40) (Figure 4). Subsequently, in December 2021, there is a slight shift towards less mafic compositions till the end of the eruption (e.g., ~7.8 and 6.1 wt% for IGN-41 and 42, respectively; Figure 4).

General trends indicate low MgO with high alkalis ($Na_2O$ ~4.2 wt% and $K_2O$ ~1.7–1.8 wt%), $TiO_2$ (~3.75 wt%), and $Al_2O_3$ contents (~14.5 wt%) in lavas from the onset of the eruption (samples IGN-3a and 3b), with a gradual increase in MgO and decrease in the other listed elements as the magma transitioned to more mafic compositions. Incompatible trace elements such as Ba, Th, Rb, and the rare earth elements (REE) show the highest contents in the earliest lavas (Ba ~630 ppm, Th ~8.1 ppm, Rb ~37 ppm, and ΣREE ~448 ppm), exhibiting positive correlations with Zr (Figure 5). In contrast, compatible elements display the lowest contents in lavas from the initial days of the eruption (e.g., Ni ~56 ppm, Co ~43 ppm, Cr ~226 ppm), increasing to higher concentrations as the compositions become more mafic (e.g., Ni ~150 ppm, Co ~51 ppm, Cr ~505 ppm) (Table 1; Figure 5).

## 5.3 Olivine compositional zoning and diffusion chronometry models

The analysed olivine phenocrysts from the entire eruption have a compositional range of 69–86 Fo mol% [$Fo = 100 \times Mg/(Mg + Fe^{2+})$] with NiO varying from 0.03 to 0.27 wt% and CaO from 0.15 to 0.56 wt%. The phenocryst compositions are plotted in the CaO and NiO (wt%) vs. Fo mol% bivariate diagrams (Figure 6) where we also differentiate the eruption date to show their temporal distribution.

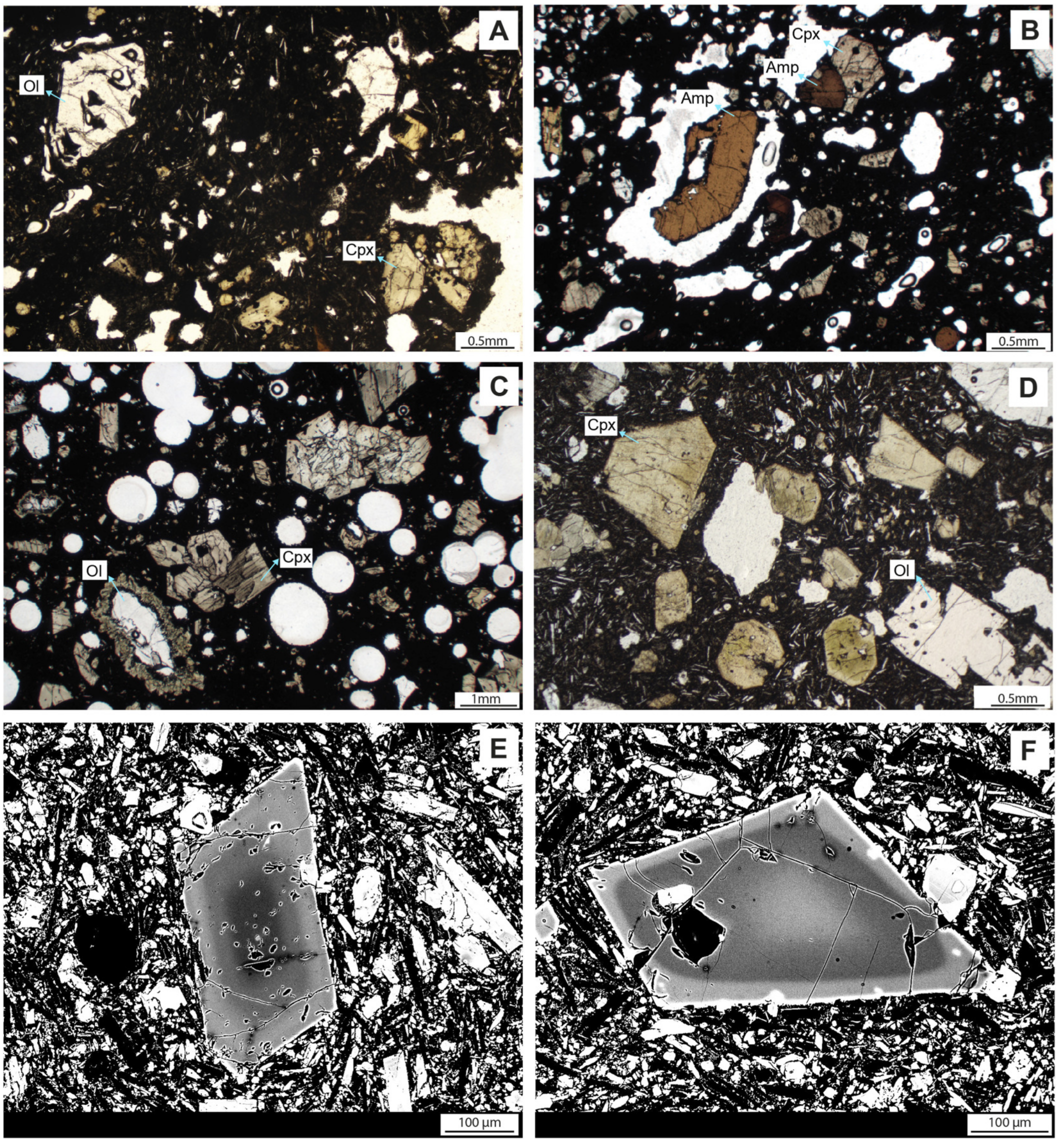

FIGURE 3
Photomicrograph of representative samples of the 2021 La Palma eruption. **(A, B)** The earliest lavas (until Day 20) with brown amphibole crystals (pleochroic) with partially resorbed rims in **(B)** and some skeletal colourless olivine embedded in a dark brown to black fine-grained groundmass. **(C)** Glomerocrysts of subhedral beige to light brown clinopyroxene, and anhedral olivine showing a thin mantle of small opaque Fe-Ti oxide and clinopyroxene microcrysts. Rounded vesicles are also shown. **(D)** Subhedral colourless olivine and euhedral to subhedral complex zoned clinopyroxene (pale to medium brown) crystals. In the studied samples, plagioclase is always restricted to the groundmass. **(E, F)** BSE images of zoning patterns in olivine crystals from the first days of the eruption (LP21-02 and LP21-04, respectively).

Lower Fo values correspond to the beginning of the eruption (LP21-02 and 04), while the highest Fo olivine crystals are hosted in the bomb erupted at the end of the eruption (LP21-94). Olivine crystals from intermediate dates show fluctuating Fo values (Figure 6).

Olivine phenocrysts are compositionally zoned, and three zoning types have been recognized: normal, reverse and complexly zoned crystals (see Figures 3E,F). Olivine crystals from the early erupted lavas differ from the rest of the samples in composition and zoning patterns. The bigger crystals (600–800 µm from rim to rim) we analysed display a reversely zoned core (from 78.5 to 80.5 Fo mol%) followed by oscillatory and sharp variations resembling those found in the early tephra erupted from the Paricutin volcano indicating the dyke opening process (compare Figures 3E, F and Fig. 1 in Albert et al. (2020). These oscillatory patterns suggest that the external part of these profiles is recording fast crystal growth with limited intra-crystal diffusion (cf. Albert et al., 2020). A smaller crystal (ca. 200 µm) from the beginning of the eruption displays, instead, normal zoning from a higher Fo core (81.7 mol%), followed by oscillations in composition toward the rim.

Olivine crystals from the subsequent lava flows show both normal and reverse zoning (shoulder-like profiles). Normally zoned olivine phenocrysts have cores at ca. 84 Fo mol% and rims below 80 Fo mol%. In contrast, cores from reversely zoned olivine crystals

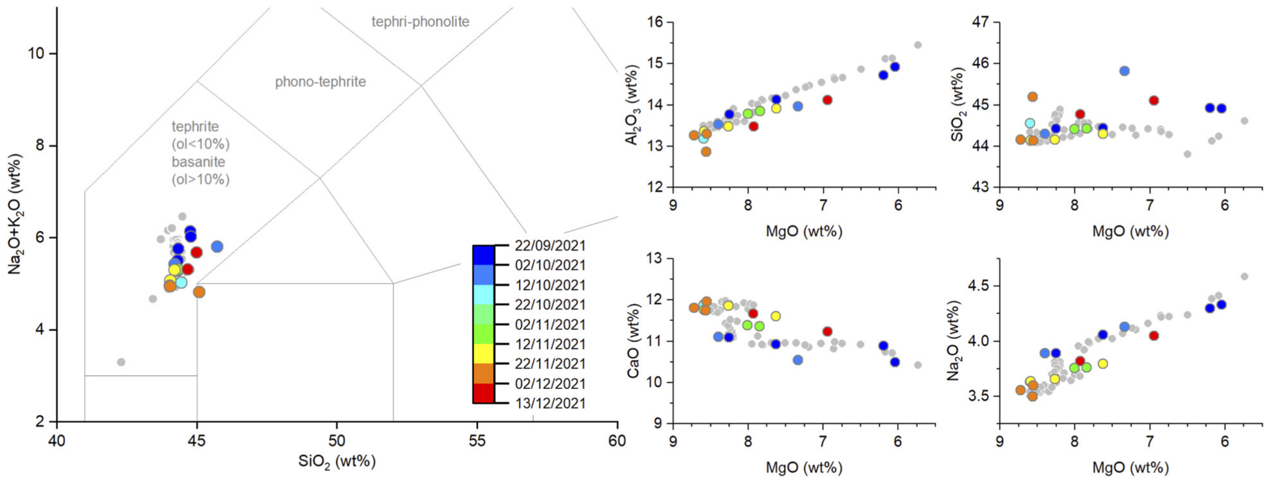

FIGURE 4
Total Alkali vs. Silica (TAS) diagram and selected major element variation diagrams for the studied samples. Data from Day et al. (2022b) have been included for comparison (grey dots). The colour palette indicates the evolution with time of the erupted magma composition (from blue to red) from MgO values of 6 wt% at the beginning of the eruption (September) to ca. 9 wt% in November, and 7–8 wt% in December.

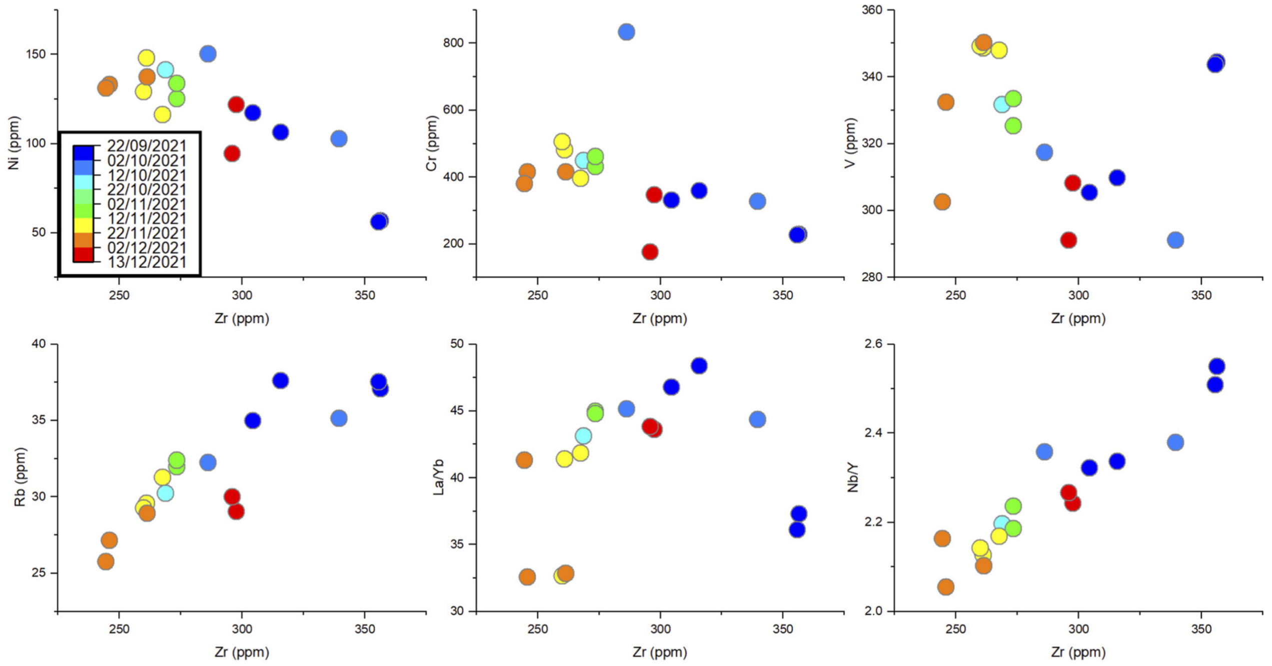

FIGURE 5
Selected trace element variation diagrams of the analysed samples. As for the major elements, the more evolved nature of the earliest erupted lavas and the transition to more mafic compositions with time can be observed from the trace elements concentration.

range from 80 to 82 mol%, mantles (shoulder) are at 83–84 Fo mol%, and external rims below 80 Fo mol%.

Ten olivine crystals were selected to calculate the timescales of the magmatic processes according to chemical diffusion. The initial and boundary conditions were chosen to represent the different core plateau compositions and the observed composition at the "shoulder," when present, and rim for Fo (Mg/Fe), Ni and Mn concentrations. Although our choice of initial and boundary conditions is non-unique, the time differences between the possible ranges of initial and boundary conditions that properly match the data are small and typically within error. Modelling of Fo, Ni and Mn zoning towards the crystal rims give consistent results (Figure 7; Table 2), with low discrepancy values and times ranging from 23 to 81 days (for nine of the ten modelled crystals; Table 2).

Calculated timescales from olivine crystals from samples LP21-65 and −77, point to the same pre-eruptive intrusion (1–2 weeks

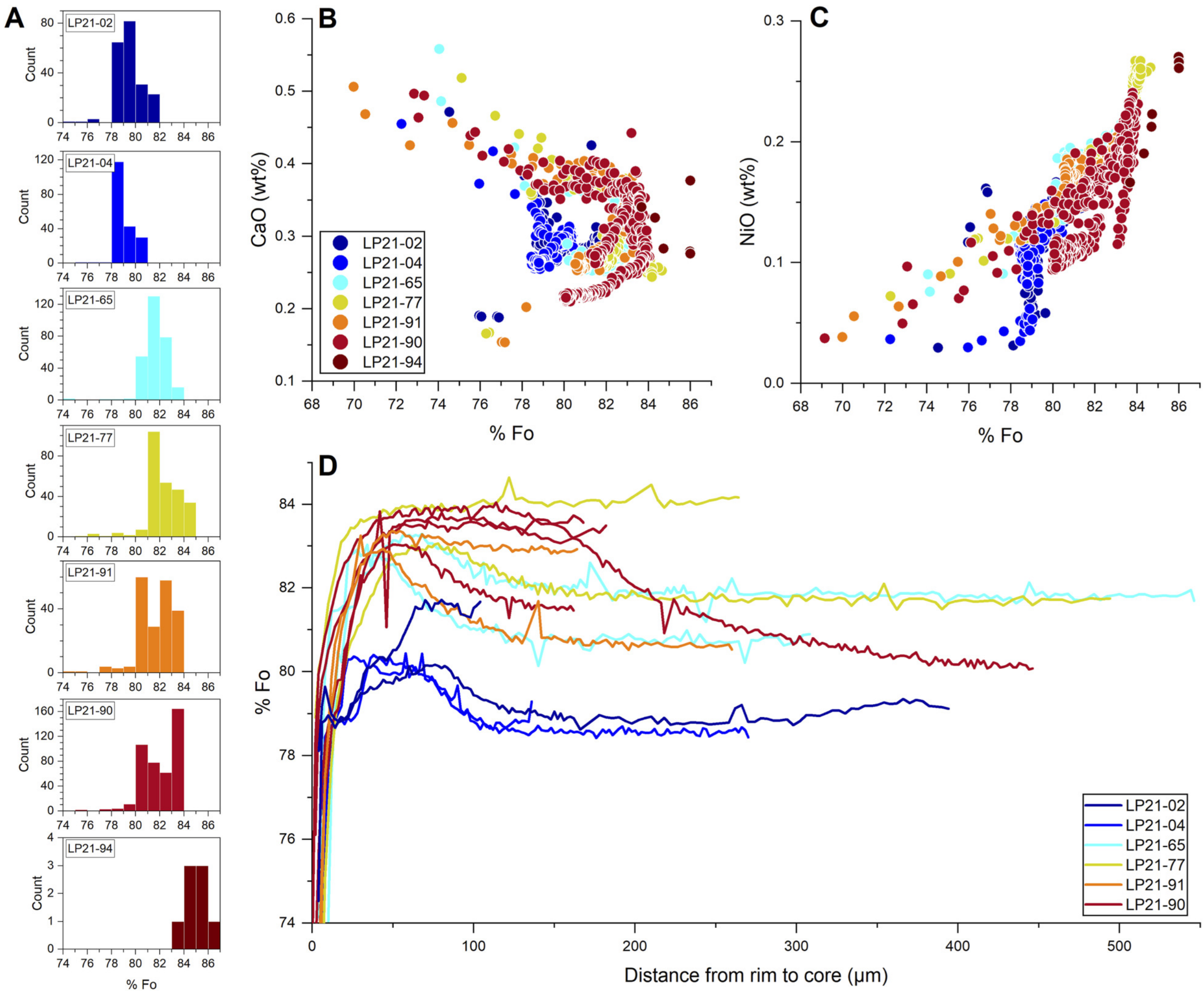

FIGURE 6
**(A)** Frequency histograms displaying the distribution of Fo (mol %) in olivine crystals from the seven selected samples (profiles and punctual analyses). **(B, C)** Fo content (mol %) vs. CaO and NiO (wt. %) for olivine crystals. Different trends can be observed for each sample. **(D)** Olivine Fo (mol %) profiles from rim to core. Lower core compositions can be found in the earliest lava, while intermediate lavas include olivine crystals with both low and high Fo cores. Zoning patterns thus vary from normal to complex.

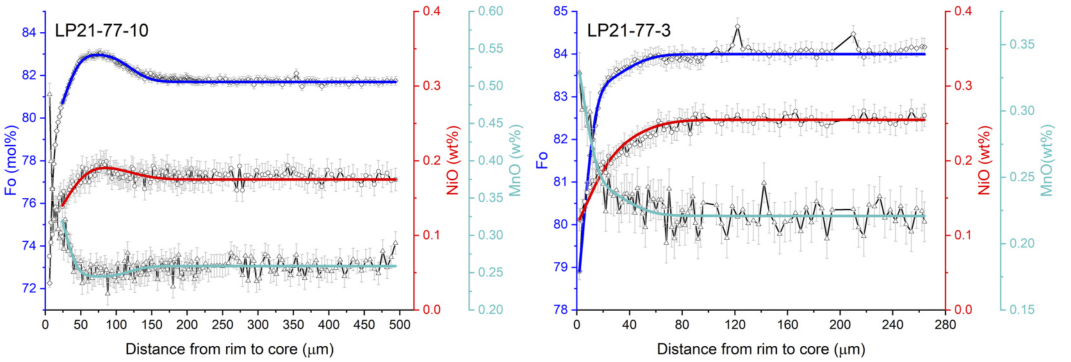

FIGURE 7
Compositional profiles (Fo, Ni and Mn) and diffusion models of two representative olivine crystals from La Palma 2021 eruption. Best-fit diffusion models were computed using DIPRA (Girona and Costa, 2013). Locations of the Fo, Ni and Mn compositional changes are consistent. The analytical errors considered for modelling are ±0.2 for the Fo (mol %) and ±0.015 for the NiO and MnO (wt. %).

before the eruption). The crystals in these samples record the mixing between two distinct magma pockets emplaced within the crust: one in equilibrium with olivine cores of Fo81-82 and the other with olivine cores of Fo84. Crystals with Fo81-82 cores exhibit reverse zoning toward Fo83 at the rim, while the crystal with a Fo84 core displays normal zoning. Notably, the olivine compositions in both cases are not consistent with primitive mantle-derived melts, supporting a scenario of interaction between magma batches that had been stored and differentiated at upper mantle and crustal levels, thus underscoring the role of shallow crustal dynamics in triggering the eruption.

Timescales retrieved from the two subsequent samples (LP21-91 and LP21-90) point to new magma injections of a more mafic crustal magma (presence of reversely zoned olivine crystals). According to the diffusion models, sample LP21-91 recorded an intrusion of a more mafic magma ca. 46 days before its eruption (i.e., middle October). Crystals from sample LP21-90 instead show a broader range of diffusion timescales, spanning from late October to mid-November, suggesting prolonged residence in a storage region undergoing continuous recharge.

One crystal hosted in the last erupted lava sample (LP21-90-2) represents an exception. The crystal has a low Fo core and the highest Fo and broadest plateau on the shoulder compared to the other crystals. From this second plateau inconsistencies between Fo, Ni and Mn are observed. This suggests a growth component that brings to the higher discrepancy value in the Fo model. The calculated timescale indicates a residence time in the system of ca. 2 years, which is a maximum time, since crystal growth contribution is neglected.

## 5.4 Dissolved gasses

From January 2019 until December 2021, dissolved helium sampled at QP63 ranged from ≤2 to 112 ± 6 ppm (Figure 8, lower panel). The maximum value was reached in April 2021 while the lowest one was measured in January 2019. Values saw an initial ascent from January (≤2 ppm) to April 2019 (32 ppm) staying stable until the beginning of 2020. Afterwards, helium values showed a sharp increase in June 2020 (92 ppm) remaining at higher values until November 2020 when values experienced a decrease. A renewed increase was then again recorded in February 2021 with helium values remaining high (97 ppm) until the eruption onset in September 2021. During the eruptive period, helium showed fluctuations but, in general, concentration values were relatively high relative to those in 2019 (39–93 ppm) and similar to those recorded in late 2020.

Regarding carbon dioxide concentration (Figure 8, lower), its maximum value was recorded on 3 November 2021, 24.2% ± 0.7%, while the minimum was measured in January 2019, 3.8% ± 0.1%. In April 2019, $CO_2$ concentration showed its first clear increase reaching values between 11% and 13% staying in this range until the beginning of 2020. During that year, concentration values were clearly higher reaching a relative maximum in August, 22.6% ± 0.7%, and then, during 2021, carbon dioxide showed fluctuations but with a marked increase until the eruption onset. In the eruptive period, values remained at around 20% reaching a maximum in November.

## 5.5 Surface deformation

After a period without significant changes in deformation during 2019, LP06 permanent GNSS station registered an accumulated deformation of 4 mm to the east and 3 mm to the south from April to May 2020 (Figure 8). InSAR time series cannot confirm LP06 displacements during this period, likely due to the small magnitude of the deformation. Afterwards, in September 2021, during the days preceding the eruption, the main observed deformation took place in the same direction, mainly towards the east and to a lesser extent towards the south, but with much greater intensity.

On 13 September 2021, a strong deformation began to be registered in several GNSS permanent stations of the monitoring network (Figure 2). Figures 2C,D show accumulated deformations between September 8 and 20 2021 measured by InSAR. Station LP03 is located inside the maximum deformation area and very close to the eruptive centers (Figure 2C). From this day until the onset of the eruption on 19 September 2021, the deformation in LP03 was predominantly vertical. On 19 September 2021, several hours before the onset of the eruption, LP03 horizontal deformation suddenly changed towards the south reaching a total displacement of more than 2 cm to the southeast and 20 cm of vertical, since the beginning of the unrest (Figure 9). This deformation is also observed in the time series obtained using InSAR for the same area (Figure 10). Although InSAR deformation is recorded in the LOS (Line of Sight) of the satellite and is thus a composition of vertical and horizontal displacements, InSAR and GNSS vertical time series fit well, as deformations are mainly vertical.

From September 20 to 22 December 2021, a total of eight non-cumulative and transient deformation pulses were recorded in LP03, mainly as inflation in the vertical component, but also towards the south. The last of these pulses was also the longest one (4 days) and began on 19 December 2021, 6 days after the eruption ended. In the north-south component, the pulses corresponding to October 14 and 26 2021 are clearer; from this date on, a slight but continuous deformation began towards the south until the eruption ended. Since 26 October 2021, the magnitude of the pulses in this horizontal component significantly decreased.

These transient deformation pulses recorded in LP03 were not observed using InSAR. Coherence loss, due to the presence of ash, and not an appropriate time-schedule of image sampling, are probably the main causes.

## 5.6 Eruptive column height

IGN eruptive column database includes 347 records corresponding to the altitude above sea level of the top of the eruptive column, from September 20 to 13 December 2021 (Figure 9). Each observation was made at the time of detection of an appreciable change in the height of the column, so it can be assumed that the series does not significantly vary in the interval between two consecutive measurements.

The overall mean is 3,337 m.a.s.l., with a vent altitude of nearly 1,000 m.a.s.l. More records and maximum heights are concentrated in the first half of the eruptive process, showing a more unsteady behavior. Until November 1, the mean value is 3,951 m.a.s.l. and the range is 2,200–7,500 m.a.s.l. From November 1 to December 13 the

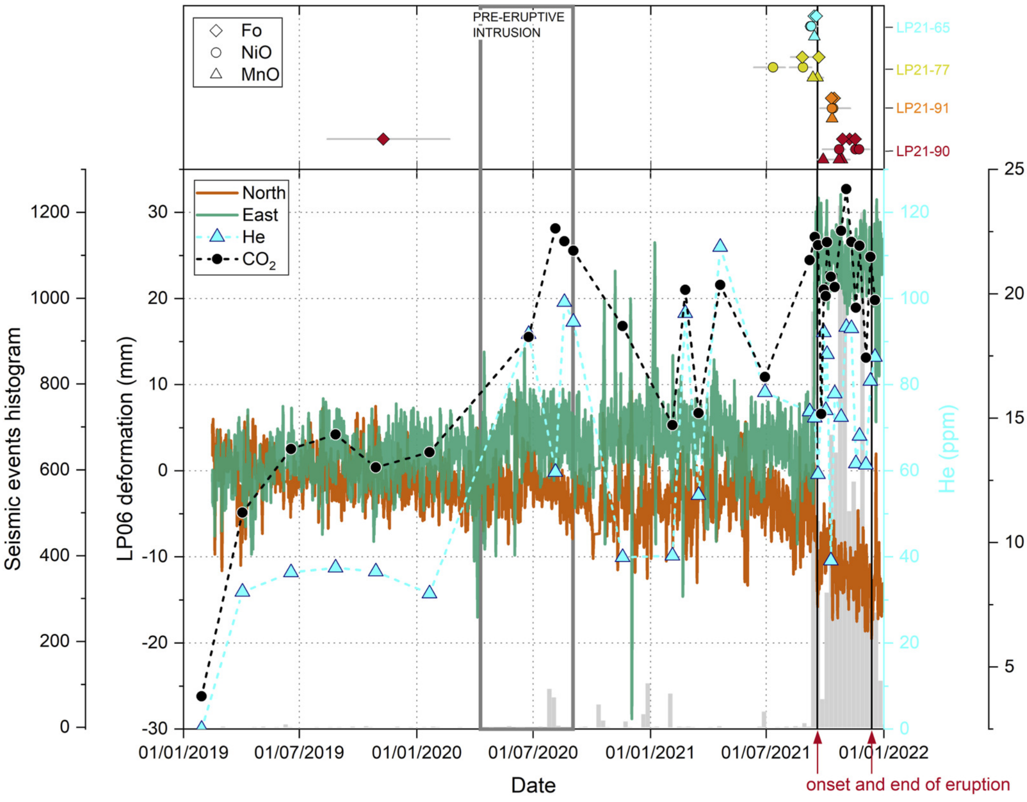

FIGURE 8
Comparison between GNSS data recorded at LP06 (red and green for North and East components, respectively), seismicity (frequency histogram plotted on the background), dissolved He and $CO_2$ (QP63), and calculated diffusion timescales (Fo, NiO and MnO content modelling) during 2019, 2020 and 2021. Black lines indicate the onset (19 September 2021) and the end (13 December 2021) of the eruptive process. The period from the beginning of April to the end of August 2020 has been highlighted (see Section 6.1). GNSS data show a slight horizontal deformation during April and May 2020, which consolidated as a permanent displacement starting in June. In September 2021, during the days preceding the eruption, the main deformation occurred in the same direction, but with much greater intensity. In the shown period, maximum concentration of dissolved $CO_2$ was reached in August 2020 when a relative maximum in dissolved He was detected. After that episode, both levels saw a decrease but did not return to previous values. Regarding He, the absolute maximum was measured in April 2021. Only one olivine crystal recording this pre-eruptive activity was found. The older date regarding the other parameters might be due to the growth component (see main text). From the other calculated timescales, at least another three intrusion episodes can be distinguished before the onset of the eruption and during the eruption itself (see Figure 10).

mean value is 2,682 m.a.s.l. and the range is 1,100–6,000 m.a.s.l., plus the maximum altitude of 8,500 m.a.s.l. achieved hours before the end of the eruption.

In addition to the onset and end of the eruption corresponding height measurements, several local maximum values were observed related to the eruptive dynamics (Figure 9). When compared to the deformation registered in LP03 GNSS, we noticed that about 5 days (mean value of 5.1 days, $\sigma = 0.57$) after every maximum value in the transient vertical displacement events detected in LP03, a maximum value in the column height was reached (see Figures 9, 10 and the Discussion section).

# 6 Discussion

## 6.1 Magmatic activity leading to eruption

### 6.1.1 Pre-eruptive activity in 2017–2018

Pre-eruptive magma intrusions occurred between 2017 and 2018 were indicated by geochemical variations in dissolved gases and seismic activity. As stated by Torres-González et al. (2020), geochemical analysis of dissolved gases showed increases in corrected $^3He/^4He$ isotopic ratio and dissolved $CO_2$ and $H_2$ concentration linked to the two seismic swarms that were registered in October 2017 and February 2018. The GNSS network did not detect any deformation during that period, which is compatible with a magma intrusion at ca. 25 km depth and an estimated maximum volume ranging between $5.5 \times 10^{-4}$ km$^3$ and $3 \times 10^{-2}$ km$^3$ (Torres-González et al., 2020). Diffusion timescales retrieved from modelling olivine crystals have not revealed such long-timescales. Nevertheless, the earlier erupted material corresponded to a more evolved magma where dominant mineral phases were clinopyroxene and amphibole. This magma might be the result of the fractional crystallization of previous intrusions at ca. 21–26 km according to seismic data of Mezcua and Rueda (2023). This magma accumulation depth matches the deep level proposed from petrological studies for the previous historical eruptions occurred in the island of La Palma (Klügel et al., 2005; Barker et al., 2015).

### 6.1.2 Pre-eruptive activity in 2019–2020

After no significant changes throughout 2019, a second magmatic activity period can be identified during 2020. LP06 GNSS

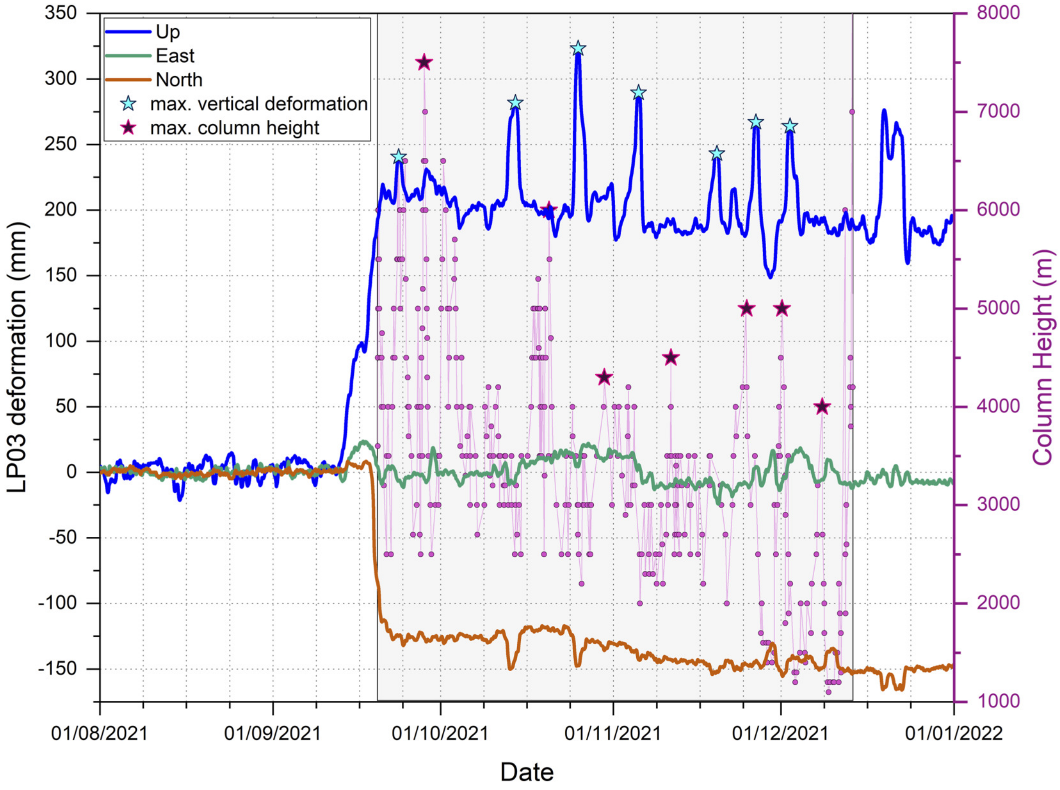

FIGURE 9
Volcanic eruption column height (m.a.s.l.) and LP03 GNSS permanent station time series from August to December 2021. The duration of the eruption is highlighted in grey. Stars indicate maximum values for vertical deformation and the eruption column height. About 5 days (5.1 days, σ = 0.57) after every maximum value in the blue line, follows a maximum value in the column height (see main text for details).

station recorded a slight surface deformation, with 4 mm horizontal displacement eastward and 3 mm southward in April and May 2020 (Figure 8), consolidated as a permanent displacement after June 2020. This horizontal deformation at LP06, predominantly eastward and to a lesser extent southward, aligns with the pressure center proposed by Torres-González et al. (2020) and is compatible with the observed deflation area associated to the drainage of a proposed reservoir at 10–15 km depth, which was active during the eruption process (del Fresno et al., 2023; Charco et al., 2024). This suggests that the observed deformation in LP06 between April and May 2020 could be related to the emplacement of a magma body and to surface inflation prior to the 2021 eruption. Furthermore, it preceded the longest seismic swarm in terms of duration and number of events before the eruption onset (long swarm number five in Mezcua and Rueda, 2023). This seismic series was located at a similar depth to that of the February 2018 swarm.

Dissolved gas analyses reveal an initial increase in He and $CO_2$ concentrations coinciding with the February 2019 swarm (long swarm number 4 in Mezcua and Rueda, 2023). Subsequent significant rises in dissolved $CO_2$ and He concentrations between February and June 2020 could be linked with the seismic activity and the deformation observed at LP06 (Figure 8). Therefore, both geophysical and geochemical data could suggest that a new magmatic intrusion took place during this time span in the same way as the 2017–2018 episode. Between the end of 2020 and the beginning of 2021, both He and $CO_2$ concentrations record a relative decline.

In the case of the 2020 intrusion, there is evidence from one olivine diffusion model. The compositional profile of crystal LP21-90-2 indicates mixing with a more mafic magma from late 2019 to early 2020. However, this large crystal exhibits both diffusion and growth based on the inconsistencies between the Fo, Ni and Mn compositional profiles, and the high discrepancy of the Fo computed timescales (Table 2). This results in an overestimation of the calculated timescale due to the crystal growth component and suggest that the mixing event might in fact fit the May 2020 intrusion recorded by the monitoring network.

### 6.1.3 Pre-eruptive activity in 2021

In December 2020 and January 2021, seismic swarms 9 and 10 (Mezcua and Rueda, 2023) were recorded at depths of 28 km and 23 km, respectively, both showing b-values of 2.1 consistent with fluid-driven processes (Mezcua and Rueda, 2023). Following these swarms, in February and April 2021, geochemical monitoring revealed two significant peaks in He concentration also accompanied by increases in $CO_2$ recorded values.

The following pre-eruptive activity episode occurred in June 2021, when a new seismic swarm was recorded. This seismic series (long swarm number 11, Mezcua and Rueda, 2023) was located at a depth of 30.2 ± 4.1 km and showed a b-value of 2.2, indicating a possible fluid contribution to the origin of that seismicity. This

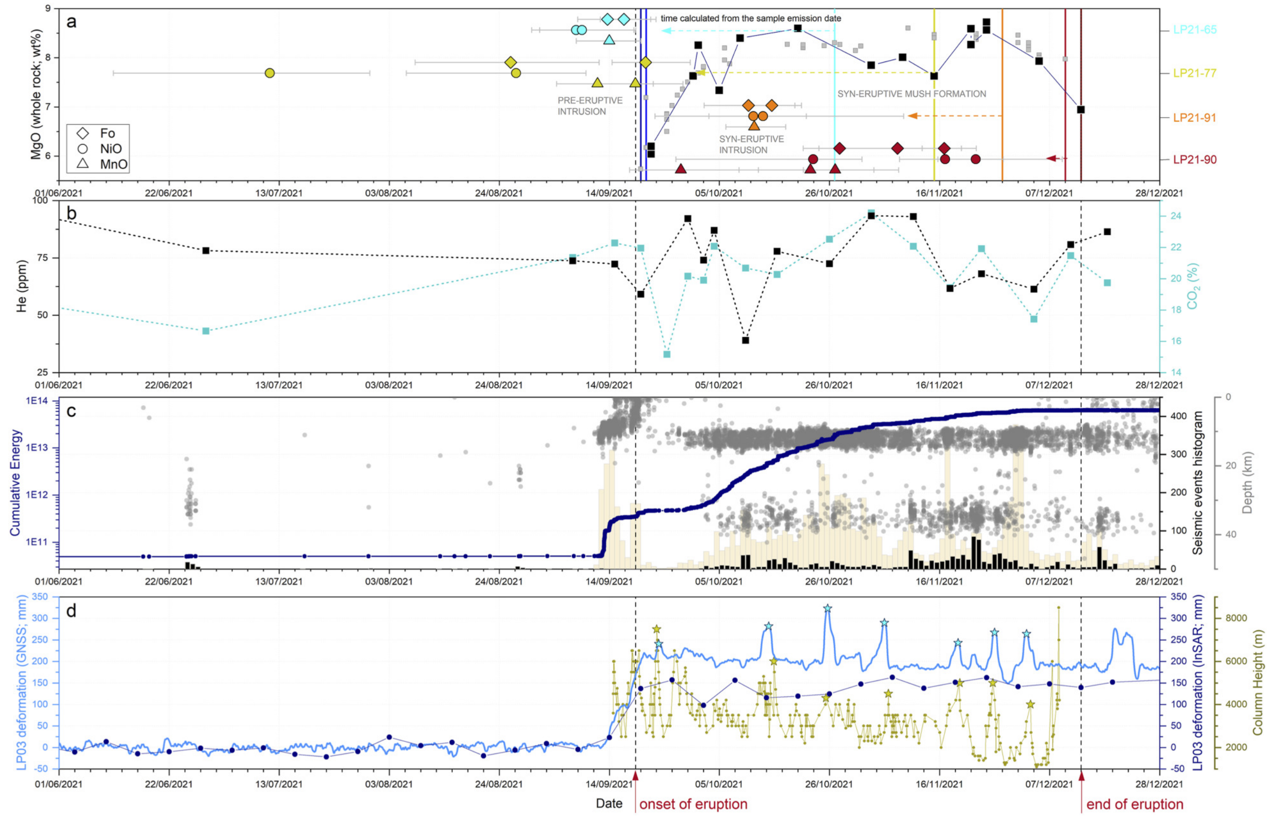

FIGURE 10
Integrated temporal evolution of magmatic and monitoring parameters during the 2021 Tajogaite eruption. **(a)** MgO content (wt.%) in whole-rock samples plotted by emission date (black and grey squares). Computed olivine diffusion timescales (Fo, NiO and MnO content modelling) are projected backward from the sample's emission date with coloured symbols corresponding to the different samples. Pre-eruptive and syn-eruptive intrusions, as well as the inferred development of a crystal mush zone, are indicated. **(b)** Temporal variations in dissolved He (black squares, left axis) and $CO_2$ (cyan squares, right axis) concentrations from groundwater at station QP63. **(c)** Seismic data including cumulative seismic energy (blue line), depth of individual seismic events (grey dots), and seismic event histograms for shallow (<15 km; yellow bars) and deep (>15 km; black bars) seismicity. **(d)** Vertical ground deformation at GNSS station LP03 (blue line, left axis) and InSAR-derived deformation (blue dots), compared with eruptive column height (yellow-green line, right axis, m.a.s.l.). Stars indicate maximums for vertical deformation and the eruption column height. The eruption column height data has been plotted after subtracting 5 days to the real date (real date can be found in Figure 9). After this modification, there is a match between the maximum values from vertical displacement and the column height (see main text).

swarm was followed by a shorter seismic series (long swarm number 12, Mezcua and Rueda, 2023) on 27 August 2021, with a shallower average depth.

About 2 weeks later, on September 11, there was an exponential increase in shallow (<15 km) seismicity, and the elevated gas (He and $CO_2$) levels were maintained. Shallow seismic events were not recorded during previous years until this day, indicating that the magma intruded during the previous episodes of magmatic activity was accumulating at the intermediate and deep pockets (Klügel et al., 2005). Since 13 September LP06 shows clear displacements towards east and south, similar to those observed during the 2020 proposed intrusion, but of higher magnitude (Figure 8).

On September 13 deformation is observed at the GNSS network, particularly in LP03 which moves mainly vertical and slightly eastwards (Figure 9). Displacements agree with the existence of a sill-like source centered below El Remo (close to the QP63 sampling point, Figure 2A) at a depth of 4 km (De Luca et al., 2022). This area is characterized by a low-density body, which could have favored the trapping of magma (Di Paolo et al., 2020; D'Auria et al., 2022; Montesinos et al., 2023). During the following days the deformation increased vertically (Figures 9, 2D) until it finally ruptured north of the station, causing sudden deformation southward on September 19, with the magma reaching the surface within hours.

On September 18, seismicity was recorded at shallower levels and began migrating northward (del Fresno et al., 2023; Suarez et al., 2023). The kink in the ascending conduit from west to north recorded by the seismicity (Figure 2) matches the location of LP03 at the vertex of the direction change. Hours before the eruption, vertical deformation at LP03 accelerated and turned south and west (Figure 9), indicating a new deformation source where magma could have pressurized for a period ranging from hours to a day before the onset of the eruption, forming an ephemeral sill located at the boundary of the low-density body (Montesinos et al., 2023). The area of maximum deformation displayed in Figures 2C,D, north of LP03, could indicate the location of this accumulation body. Following the decline recorded by the dissolved gases in 2020, there was a significant increase of the helium concentration. This gaseous species reached its maximum value, 112 ± 6 ppm, on 20 April 2021, 2 months before the June 2021 seismic series (long swarm number 11 in Mezcua and Rueda, 2023). Regarding the carbon dioxide concentration, during the same time span, it showed a synchronized trend with the helium concentration marking a clear increase.

These similar signals, expected due to their deep origins (cf. Federico et al., 2023; Rizzo et al., 2008; Scarpa et al., 1996), increased as the eruption date approached, indicating an intensification of a magmatic contribution with ongoing magma emplacement, ascent, and/or degassing (Torres-González et al., 2020).

The diffusion timescales calculated from olivine crystals in samples LP21-65 and LP21-77, which were erupted on October 27 and November 15 respectively, indicate a pre-eruptive magma intrusion that ultimately triggered the eruption. These lava samples exhibit a predominant group of crystals with reverse zoning and a subordinate group with normal zoning. The "shoulders" in the reversely zoned crystals, showing higher Fo values than their cores, align with the Fo core values of the normally zoned crystals. The ratio between these two crystal families might indicate that the volume of the intruded magma was smaller than the magma already presents in the crust, but was sufficient to destabilize the system and trigger the eruption on September 19. According to the calculated diffusion times, this intrusion occurred between August 26 and September 20 (±10 days) for 91% of the calculated times.

## 6.2 Syn-eruptive magmatic activity

Olivine crystals from the lavas emitted on September 20 and 21 (LP21-02 and LP21-04, respectively) were not considered for diffusion modelling because their zoning patterns were strongly affected by crystal growth (see Section 5.3). Oscillatory zoning recorded in the earliest olivine crystals (Figure 3) are interpreted as witnesses of the magma transport towards the surface during the conduit opening (recorded by the oscillatory zoning in the external part of the profiles), as they resemble those from the Paricutin earliest tephra (Figure 1 in Albert et al., 2020) where the dyke inception process was recorded.

Timescales retrieved from olivine crystals emitted on October 27 and November 15 have already been discussed in the previous section, as they indicated a pre-eruptive intrusion. In the same manner as the pre-eruptive timescales were calculated, crystals collected in samples LP21-91 and LP21-90 (emitted on November 28 and December 10, respectively) have given timescales that coincide with the eruptive period, indicating new deep intrusions that rejuvenized the system during the eruption itself. Following the onset of the eruption, a new intrusion was identified between October 10 and 15, based on diffusion timescales in reversely zoned olivine crystals from sample LP21-91. This intrusion is corroborated by the elevated concentrations of elements such as Mg and Ni in the whole-rock analysis. Initially, the eruption emitted magma with low concentrations of typical mafic magma elements (e.g., ca. 6 wt% Mg and 55 ppm Ni). The content of these elements gradually increased during the early days of the eruption, likely due to an increasing proportion of deep magma relative to the more evolved magma previously emplaced in the crust. After a brief decline or stabilisation in these element concentrations in early October, an increase was recorded on October 8 (ca. 8 wt% Mg and 135 ppm Ni), which aligns with the diffusion timescales calculated in the olivine crystals.

During the eruption, both He and $CO_2$ concentrations at QP63 showed a similar trend, with no significant changes except for (1) the minimum values recorded on September 25, possibly related to the temporary halt in the eruption (Taddeucci et al., 2023; Ubide et al., 2023); and (2) the peak values detected on November 3. Our diffusion timescales from one crystal in sample LP-21-90, emitted on December 10, point to a magma intrusion occurring around October 27, which followed a period of intense seismicity. The intrusion event aligns with the maximum He and $CO_2$ values measured on November 3, supporting the interpretation of a more mafic magma injection at the beginning of November (Ubide et al., 2023; Zanon et al., 2024).

During the eruptive process LP03 experienced eight sudden inflation episodes (being the last one 30 days after the end of the eruption) with the vertical component increasing by more than 10 cm in a matter of hours before returning to the base level after each event (Figure 10). The transient peaks at LP03 are considered genuine rather than noise, as they occurred both during and after the eruption. This behaviour suggests the presence of a pressurised area north of LP03 (Figure 2D), which, given the low densities at shallow depths, could be quite ductile (Montesinos et al., 2023). This would explain the significant vertical deformations observed at LP03 and the absence of associated seismicity. The second and third peaks in vertical deformation at LP03, recorded on October 14 and 25 respectively (Figure 9), coincide with two peaks in the southward displacement. We interpret these signals as representing the largest deep material intrusions. These dates align with the calculated times from the crystals (October 10–15 and October 27) and the behaviour of the dissolved gases. Following these intrusions, the system experienced a shift, as subsequent vertical deformation peaks at LP03 were no longer accompanied by peaks in southward displacement (Figure 9). Additionally, the northward component of deformation did not recover, while vertical deformation continued to show peaks. This suggests a change in the magmatic system dynamics from a regime of magma recharge and outflow to one of magma stagnation. This accumulation is consistent with the timescales derived from the olivine crystals. Whereas the timescales for earlier intrusions were clustered around specific dates, those obtained from approximately November 1 from sample LP21-90 extended over several weeks. We propose that during this stage of the eruption a small shallow mush where crystals resided for some time before being expelled was developed.

The syn-eruptive intrusions inferred from timescales calculations are consistent with previous works (Ubide et al., 2023; Dayton et al., 2024; Zanon et al., 2024), who also emphasize that the eruption was driven by discrete, repeated injections of new magma rather than a single recharge event. Together, these studies support a dynamic magmatic system involving multiple replenishments, which influenced both the eruptive behavior and magma evolution during the eruption.

The comparison of vertical deformation at LP03 with the eruptive column height reveals a mean time lag of 5.1 days ($\sigma = 0.57$) between the peaks of deformation and peaks in the maximum height of the eruptive column (Table 3). In the provided graph (Figure 10), the column height data have been adjusted by subtracting a 5-day temporal offset, with peaks in deformation

TABLE 3 Temporal differences between eruptive column height maxima and vertical deformation maxima.

| Date | Time | Day of year (DOY) | Column height (m) | Date | Time | Day of year (DOY) | Deformation (m) | Difference in DOY |
|---|---|---|---|---|---|---|---|---|
| 28 September 2021 | 1:30:00 | 2,710,625 | 7,500 | 23 September 2021 | 11:01:30 | 266,459,375 | 0.2407 | 4.60 |
| 20 October 2021 | 9:41:00 | 293,403,472 | 6,000 | 14 October 2021 | 9:55:00 | 287,413,194 | 0.2818 | 5.99 |
| 30 October 2021 | 8:29:00 | 303,353,472 | 4,300 | 25 October 2021 | 16:18:00 | 298,679,167 | 0.3232 | 4.67 |
| 11 November 2021 | 6:19:00 | 315,263,194 | 4,500 | 05 November 2021 | 11:51:00 | 30,949,375 | 0.2896 | 5.77 |
| 24 November 2021 | 20:44:00 | 328,722,917 | 5,000 | 19 November 2021 | 12:38:00 | 323,526,389 | 0.2432 | 5.20 |
| 01 December 2021 | 3:50:00 | 335,159,722 | 5,000 | 26 November 2021 | 12:06:00 | 330,504,167 | 0.2671 | 4.66 |
| 07 December 2021 | 8:00:00 | 341,373,611 | 4,000 | 02 December 2021 | 14:15:00 | 33,659,375 | 0.2640 | 4.78 |
| | | | | | | | Mean | 5.10 |
| | | | | | | | Standard deviation | 0.57 |

and adjusted column height marked by stars (original column height data can be found in Figure 9). This alignment supports the hypothesis that the deformation peaks at LP03 were associated with the accumulation of magma batches in the area beneath it. The observed delay of approximately 5 days before the eruptive column peaks suggests that these magma batches reached the surface shortly after each deformation peak, likely contributing to increased emission rates, fragmentation, and eruption intensity. This phenomenon is likely due to the presence of a kink in the conduit that aligns with the vertical position of LP03 and that promotes the accumulation of magma (Di Paolo et al., 2020; Fernández et al., 2022; Montesinos et al., 2023; Suarez et al., 2023). Similar patterns have been documented in studies of dykes in New Zealand (Wadsworth et al., 2015; Goldman et al., 2022) and the temporal correlation between the deformation peaks at LP03 and the subsequent eruptive column height maxima reinforces the idea that the deformation events were precursors to an increase in volcanic activity (Hreinsdóttir et al., 2014; Spina et al., 2017; Benito et al., 2023).

On late November a decrease in mafic elements in the whole-rock composition (e.g., Mg in Figure 10) is detected. After this date, no diffusion timescales in olivine were recorded. This marks a critical inflection point in the eruption, likely representing the last intrusion that managed to be expelled. Previous intrusions had reset the system by introducing mafic material, but from this point onwards, the magma composition became progressively more evolved. This interpretation aligns with previous studies that identify a shift at the end of November from deep magma recharge to the evacuation of more evolved, residual melts. Authors such as Ubide et al. (2023), Zanon et al. (2024) or Scarrow et al. (2024) point to this transition as initiating the shutdown of the magmatic system.

## 6.3 Comparison with the San Juan (1949) and Teneguía (1971) eruptions

Our results from the 2021 Tajogaite eruption highlight differences and similarities with previous eruptions at Cumbre Vieja, particularly the 1949 San Juan and the 1971 Teneguía events. The 1949 eruption involved the widest spatial distribution of vents among historical Cumbre Vieja eruptions and produced a diverse range of erupted materials, including both primitive mantle xenoliths and more evolved products (phono-tephrite), exceeding the compositional diversity observed in the 1971 and 2021 events. Unlike the 1949 eruption, the olivine compositions (Fo81–84) from the 2021 eruption and the absence of mantle signatures suggest that the Tajogaite eruption was fuelled by shallow to intermediate upper mantle and crustal magma pockets, rather than by direct input of primitive mantle melts. The 1971 Teneguía eruption, like Tajogaite, initially emitted basanite containing amphibole, followed by a less evolved, more mafic basanite during a second phase reflecting a similar transition in magma composition over time.

Importantly, the pre-eruptive timescales inferred from olivine diffusion in the 2021 eruption are comparable to the long timescales of unrest prior to the 1949 eruption, which included over 2 years of seismicity. In contrast, the 1971 eruption was preceded by much shorter periods of seismic unrest, but to date no diffusion chronometry studies are available to constrain the timescales of pre-eruptive processes for the 1971 eruption event.

These comparisons emphasize that, while certain magmatic processes (e.g., magma mixing and the transition from evolved to less evolved basanites) recur in Cumbre Vieja eruptions, monogenetic eruptions in this volcanic field can display significant variability in terms of pre-eruptive unrest duration, spatial

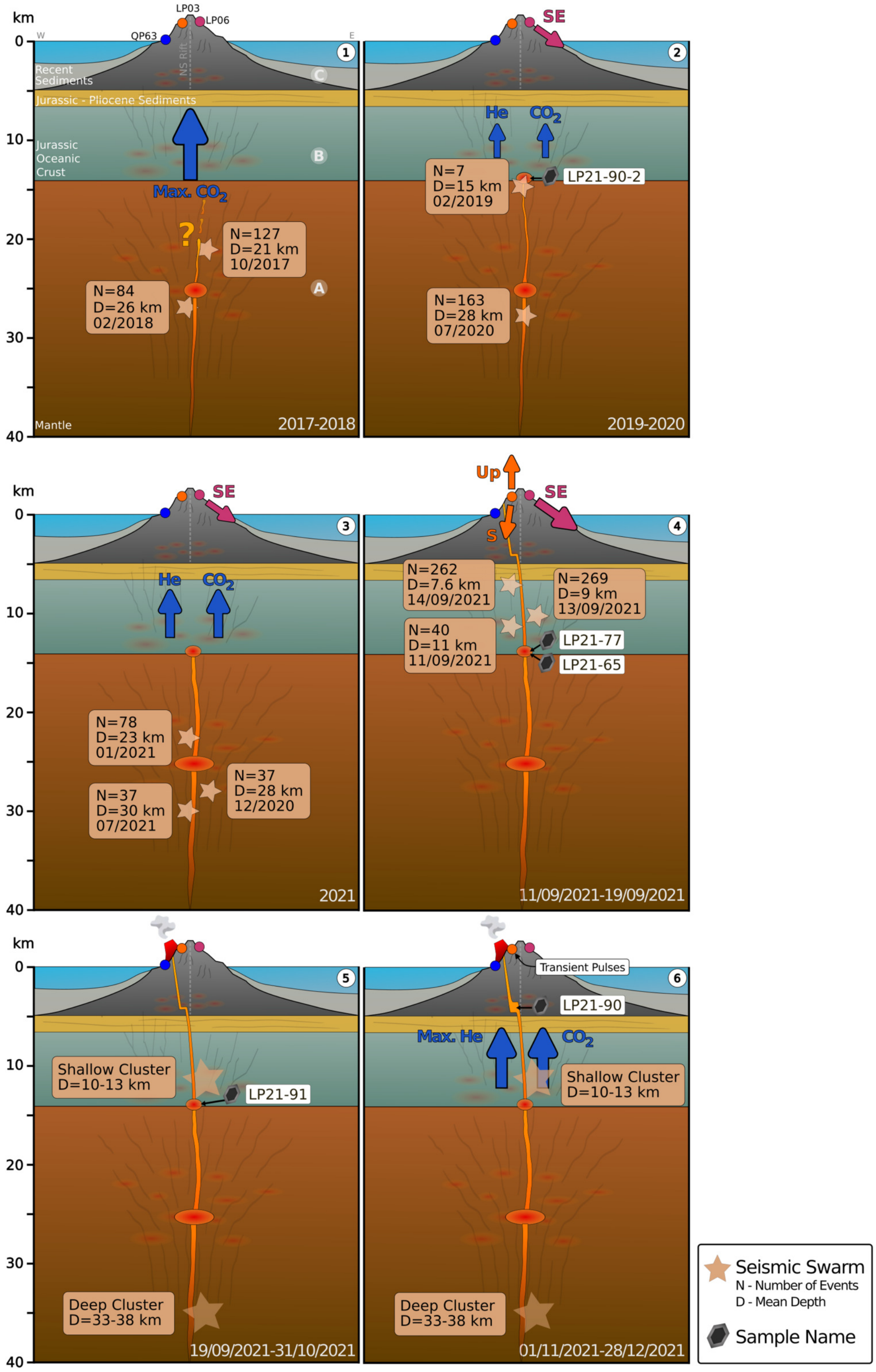

FIGURE 11
Schematic cross-sections illustrating six key time lapses before and during the eruption. The seismic swarms are indicated as brown stars. For each swarm a label is included with the date, N standing for the number of events and D for the mean depth (del Fresno et al., 2023; Mezcua and Rueda, 2023). Blue arrows indicate $CO_2$ and He gas emissions at the QP63 sampling point (their size indicates the relative intensity). Grey hexagons stand for the olivine samples used to calculate diffusion timescales (sample name next to them). Deformation rates indicating the main direction are represented by pink (LP06) and orange (LP03) arrows. Different earth layers are indicated: mantle, Jurassic oceanic crust, Jurassic-Pliocene sediments and recent sediments. The diagram integrates petrological, geochemical, and geophysical observations (from this study and from Torres-González et al., 2020; del Fresno et al., 2023; Mezcua and Rueda, 2023), highlighting the sequence of intrusions and crustal processes that culminated in the 2021 eruption and the formation of a shallow crystal mush.

concentration of eruptive vents, eruptive styles, and the composition (and therefore behavior) of the erupted products. Consequently, the associated volcanic hazard can differ from one eruption to another, highlighting the need for event-specific monitoring and risk assessment strategies.

### 6.4 Implications of real-time petrological monitoring and future perspectives on magma storage and eruption termination

Importantly, we emphasize that if the 2021 Tajogaite eruption had not been monitored in real time, all diffusion timescales derived from olivine crystals would have been calculated backward from the start of the eruption, treating it as a fixed reference point. Under such conditions, the timescales would have converged on a single pre-eruptive intrusion event around mid-August, without resolving the distinct pulses of magma input that we have identified through integrated petrological and geophysical observations. This underscores a critical limitation in studying past eruptions where the precise timing of each eruptive level is unknown. The temporal resolution achieved in this study, by linking individual crystal zoning patterns to specific eruptive events, would have been impossible without direct monitoring of eruptive activity, highlighting the unique value of real-time petrological surveillance in understanding the evolution of active volcanic systems.

The 2021 Tajogaite eruption on La Palma provided an extensive dataset that has significantly advanced our understanding of volcanic processes, their preceding unrest episodes, and the syn-eruptive processes leading to changes in the eruptive behaviour. Future investigations could address whether the formation of a proto-crystal mush played a role in terminating the eruption by facilitating the accommodation and storage of ascending magma without its eruption. It is also important to consider how the eruptive behaviour evolved following the establishment of this mush zone, as it may significantly influence the dynamics of future events.

## 7 Summary and conclusions

We have constructed a temporal schematic diagram of key events and processes in the form of a timeline with annotated vignettes (Figure 11) to illustrate the following conclusions:

- Although diffusion timescales from olivine crystals did not record the magmatic intrusion that occurred between 2017 and 2018 (evidenced by geochemical and seismic signals; Figure 11) the early erupted material, dominated by clinopyroxene and amphibole, suggests a more evolved magma, likely formed through fractional crystallization of earlier intrusions at intermediate crustal depths.
- A magmatic intrusion took place in 2020, supported by deformation recorded at GNSS station LP06 and increased concentrations of dissolved He and $CO_2$. The long diffusion timescale from one olivine crystal may reflect this intrusion, although crystal growth likely overestimates the actual residence time. The crystal's zoning pattern indicates interactions between likely crustal magma pockets that had been previously intruded (Fo reverse zoning from 80 to 84), rather than a direct input from a primitive mantle source.
- An intrusion, immediately preceding the 2021 eruption, is implied by seismicity, gas emissions, and ground deformation. Diffusion modelling of olivine crystals erupted during the end of October and beginning of November, suggests that this intrusion occurred between late August and mid-September, triggering the eruption. Once again, olivine crystals do not record a direct mantle source; instead, their compositions (both at the cores and rims) indicate crystallization from magmas residing in the crust, reflecting interactions among shallow magma pockets rather than primitive mantle-derived melts.
- Early erupted olivine crystals (first days of the eruption) exhibit oscillatory zoning patterns, likely recording conduit opening and rapid magma ascent during dyke propagation. These crystals are the most evolved (core at Fo79) of the entire eruption and are hosted in the most differentiated rocks of the eruptive sequence. Their crystallization occurred during the initial dyke opening and magma ascent, following the mixing of an intermediate magma (characterized by pyroxene and amphibole as dominant phases) with a subordinate volume of more mafic magma.
- Olivine crystals erupted at the end of November record an additional magmatic intrusion that occurred in mid-October. This mixing event is reflected in the higher Mg content (as well as other mafic elements) in whole-rock compositions and coincides with an increase in deep seismicity.
- Following this intrusion, an increase in shallow seismicity was observed, accompanied by a series of deformation pulses recorded at GNSS station LP03. These pulses were consistently followed, after approximately 5 days, by peaks in the eruptive column height, suggesting a lag between magma intrusion, accumulation, and subsequent eruptive intensification. Olivine crystals erupted during the final days of the eruption registered a wider range of diffusion timescales, spanning from late October to mid-November. This likely indicates residence time in a storage region affected by continued recharge and without an immediate eruption. During this phase, the magma accumulation area in the upper crust appears to have transitioned into the development of a proto-crystal mush zone. This interpretation is supported by the extended olivine residence times and the consistent ca. 5-day lag between deformation peaks at LP03 and subsequent maxima in eruptive column height pointing to episodes of magma accumulation within the developing crystal mush, pressurization, and delayed surface ejection.
- After late November, mafic element concentrations declined and no further diffusion timescales were retrieved from olivine, indicating a shift to more evolved magma and the cessation of deep magma input.
- The integrated use of petrological, geochemical, and geophysical monitoring is a powerful tool for identifying magma recharge events and understanding the temporal evolution of the volcanic system. Our findings thus highlight the importance of multi-disciplinary surveillance to detect the formation of crustal mushes and to improve eruption forecasting in monogenetic volcanic fields.

## Data availability statement

The original contributions presented in the study are included in the article/Supplementary Material, further inquiries can be directed to the corresponding author.

## Author contributions

HA: Conceptualization, Data curation, Formal Analysis, Funding acquisition, Investigation, Methodology, Project administration, Resources, Visualization, Writing – original draft, Writing – review and editing. PT: Conceptualization, Data curation, Formal Analysis, Investigation, Methodology, Resources, Visualization, Writing – original draft, Writing – review and editing. HL: Data curation, Formal Analysis, Investigation, Methodology, Visualization, Writing – original draft, Writing – review and editing. VV: Conceptualization, Data curation, Formal Analysis, Investigation, Methodology, Resources, Visualization, Writing – original draft, Writing – review and editing. NL: Conceptualization, Data curation, Formal Analysis, Investigation, Methodology, Resources, Visualization, Writing – original draft, Writing – review and editing. AF: Data curation, Formal Analysis, Investigation, Methodology, Visualization, Writing – original draft, Writing – review and editing. AM: Data curation, Formal Analysis, Investigation, Methodology, Visualization, Writing – original draft, Writing – review and editing. MA: Funding acquisition, Investigation, Resources, Visualization, Writing – original draft, Writing – review and editing. EG: Data curation, Formal Analysis, Investigation, Methodology, Visualization, Writing – original draft, Writing – review and editing. FP: Data curation, Formal Analysis, Investigation, Methodology, Visualization, Writing – original draft, Writing – review and editing. GG: Resources, Writing – review and editing. VT: Resources, Writing – review and editing.

## Funding

The author(s) declared that financial support was received for this work and/or its publication. This research was funded by the following projects: PROMEDED (PID 2019-104624RB-I00; Ministerio de Ciencia, Innovación y Universidades), LAJIAL (PGC 2018-101027-B-I00, MCIU/AEI/FEDER, EU), MESVOL (SD RD 1078/2021 LA PALMA), and DYNAMICS (PID 2023-151693NA-I00 funded by MCIN/AEI/10.13039/501100011033 and by 'ERDF A way of making Europe').

## Acknowledgements

We are grateful to Francisca Martínez Ruiz and Amparo Salido Ruiz (researcher and XRF technician at the Instituto Andaluz de Ciencias de la Tierra, respectively) for their help with major and trace element analysis of IGN set of rock samples. We also acknowledge Xavier Llovet for his assistance during EPMA analyses.

## Conflict of interest

The author(s) declared that this work was conducted in the absence of any commercial or financial relationships that could be construed as a potential conflict of interest.

## Generative AI statement

The author(s) declared that generative AI was not used in the creation of this manuscript.

Any alternative text (alt text) provided alongside figures in this article has been generated by Frontiers with the support of artificial intelligence and reasonable efforts have been made to ensure accuracy, including review by the authors wherever possible. If you identify any issues, please contact us.

## Publisher's note

## Supplementary material

The Supplementary Material for this article can be found online at: https://www.frontiersin.org/articles/10.3389/feart.2026.1677805/full#supplementary-material

## References

Afonso, A., Aparicio, A., Hernández-Pacheco, A., and Badiola, E. R. (1974). Morphology evolution of Teneguía volcano area. *Estud. Geol.*, 19–26.

Albert, H., Costa, F., and Martí, J. (2015). Timing of magmatic processes and unrest associated with mafic historical monogenetic eruptions in Tenerife Island. *J. Petrology* 56, 1945–1966. doi:10.1093/petrology/egv058

Albert, H., Costa, F., and Martí, J. (2016). Years to weeks of seismic unrest and magmatic intrusions precede monogenetic eruptions. *Geology* 44, 211–214. doi:10.1130/G37239.1

Albert, H., Costa, F., Di Muro, A., Herrin, J., Métrich, N., and Deloule, E. (2019). Magma interactions, crystal mush formation, timescales, and unrest during caldera collapse and lateral eruption at ocean island basaltic volcanoes (Piton de la Fournaise, La Réunion). *Earth Planet Sci. Lett.* 515, 187–199. doi:10.1016/j.epsl.2019.02.035

Albert, H., Larrea, P., Costa, F., Widom, E., and Siebe, C. (2020). Crystals reveal magma convection and melt transport in dyke-fed eruptions. *Sci. Rep.* 10, 1–10. doi:10.1038/s41598-020-68421-4

Albert, H., Trua, T., Fonseca, J., Marani, M. P., Gamberi, F., Spiess, R., et al. (2022). Time scales of open-system processes in a complex and heterogeneous mush-dominated plumbing system. *Geology* 50, 869–873. doi:10.1130/G49934.1

Altamimi, Z., Rebischung, P., Métivier, L., and Collilieux, X. (2016). ITRF2014: a new release of the International Terrestrial Reference Frame modeling nonlinear station motions. *J. Geophys Res. Solid Earth* 121, 6109–6131. doi:10.1002/2016JB013098

Ancochea, E., Hernán, F., Cendrero, A., Cantagrel, J. M., Fúster, J., Ibarrola, E., et al. (1994). Constructive and destructive episodes in the building of a young Oceanic Island, La Palma, Canary Islands, and genesis of the Caldera de Taburiente. *J. Volcanol. Geotherm. Res.* 60, 243–262. doi:10.1016/0377-0273(94)90054-X

Aoki, Y., Takeo, M., Nagaoka, Y., and Nishida, K. (2013). Magma pathway and its structural controls of asama volcano, Japan. *Geol. Soc. Spec. Publ.* 380, 67–84. doi:10.1144/SP380.6

Araña, V. (1999). Comentarios sobre la erupción del volcán Teneguía en 1971. *Enseñanzas las Ciencias la Tierra* 7, 262–266.

Araña, V., and Fuster, J. (1974). La erupción del volcán Teneguía, La Palma, Islas Canarias, 1971. *Estud. Geol.*, 15–18.

Barde-Cabusson, S., Gottsmann, J., Martí, J., Bolós, X., Camacho, A. G., Geyer, A., et al. (2014). Structural control of monogenetic volcanism in the Garrotxa volcanic field (Northeastern Spain) from gravity and self-potential measurements. *Bull. Volcanol.* 76, 1–13. doi:10.1007/s00445-013-0788-0

Barker, A. K., Troll, V. R., Carracedo, J. C., and Nicholls, P. A. (2015). The magma plumbing system for the 1971 Teneguía eruption on La Palma, Canary Islands. *Contributions Mineralogy Petrology* 170, 1–21. doi:10.1007/s00410-015-1207-7

Benito, M. B., Alvarado, G. E., Marchamalo, M., Rejas, J. G., Murphy, P., Franco, R., et al. (2023). *Temporal and spatial evolution of the 2021 eruption in the Tajogaite volcano (Cumbre Vieja rift zone, La Palma, Canary Islands) from geophysical and geodetic parameter analyses*. Netherlands: Springer. doi:10.1007/s11069-023-06090-y

Berardino, P., Fornaro, G., Lanari, R., and Sansosti, E. (2002). A new algorithm for surface deformation monitoring based on small baseline differential SAR interferograms. *IEEE Trans. Geoscience Remote Sens.* 40, 2375–2383. doi:10.1109/TGRS.2002.803792

Berthod, C., Médard, E., Bachèlery, P., Gurioli, L., Di Muro, A., Peltier, A., et al. (2021). The 2018-ongoing Mayotte submarine eruption: magma migration imaged by petrological monitoring. *Earth Planet Sci. Lett.* 571, 117085. doi:10.1016/j.epsl.2021.117085

Bindeman, I. N., Deegan, F. M., Troll, V. R., Thordarson, T., Höskuldsson, Á., Moreland, W. M., et al. (2022). Diverse mantle components with invariant oxygen isotopes in the 2021 Fagradalsfjall eruption, Iceland. *Nat. Commun.* 13, 3737. doi:10.1038/s41467-022-31348-7

Blundy, J., and Cashman, K. (2008). Petrologic reconstruction of magmatic system variables and processes. *Rev. Mineral. Geochem* 69, 179–239. doi:10.2138/rmg.2008.69.6

Bonechi, B., Polacci, M., Arzilli, F., Romero, J. E., Fellowes, J., and Burton, M. (2024). Magma residence time, ascent rate and eruptive style of the November ash-laden activity during the 2021 Tajogaite eruption (La Palma, Spain). *Volcanica* 7, 51–65. doi:10.30909/vol.07.01.5165

Bonelli Rubio, J. M. (1950). *Contribución al estudio de la erupción del volcán del Nambroque o San Juan (Isla de la Palma), 24 de Junio - 4 de Agosto de 1949*. Madrid, Spain: Talleres del Instituto Geográfico y Catastral.

Burton, M., Aiuppa, A., Allard, P., Asensio-Ramos, M., Cofrades, A. P., La Spina, A., et al. (2023). Exceptional eruptive CO2 emissions from intra-plate alkaline magmatism in the Canary volcanic archipelago. *Commun. Earth Environ.* 4, 1–10. doi:10.1038/s43247-023-01103-x

Cannavò, F., Camacho, A. G., González, P. J., Mattia, M., Puglisi, G., and Fernández, J. (2015). Real time tracking of magmatic intrusions by means of ground deformation modeling during volcanic crises. *Sci. Rep.* 5, 10970. doi:10.1038/srep10970

Capasso, G., and Inguaggiato, S. (1998). A simple method for the determination of dissolved gases in natural waters. An application to thermal waters from Vulcano Island. *Appl. Geochem.* 13, 631–642. doi:10.1016/S0883-2927(97)00109-1

Caracciolo, A., Bali, E., Halldórsson, S. A., Guðfinnsson, G. H., Kahl, M., Þórðardóttir, I., et al. (2023). Magma plumbing architectures and timescales of magmatic processes during historical magmatism on the Reykjanes Peninsula, Iceland. *Earth Planet Sci. Lett.* 621, 118378. doi:10.1016/j.epsl.2023.118378

Carbone, D., and Greco, F. (2007). Review of microgravity observations at Mt. Etna: a powerful tool to monitor and study active volcanoes. *Pure Appl. Geophys* 164, 769–790. doi:10.1007/s00024-007-0194-7

Carracedo, J. C., and Troll, V. R. (2016). *The geology of the Canary Islands*. Elsevier. doi:10.1007/978-94-010-1566-0_4

Carracedo, J. C., Badiola, E. R., Guillou, H., De La Nuez, J., and Pérez Torrado, F. J. (2001). Geology and volcanology of La Palma and El Hierro, Western Canaries. *Estud. Geol.* 57, 175–273. doi:10.3989/egeol.01575-6134

Carracedo, J. C., Troll, V. R., Day, J. M. D., Geiger, H., Junca, M. A., Soler, V., et al. (2022). The 2021 eruption of the Cumbre Vieja Volcanic Ridge on La Palma, Canary Islands. *Geol. Today* 38, 94–107. doi:10.1111/gto.12388

Cashman, K. V., and Edmonds, M. (2019). Mafic glass compositions: a record of magma storage conditions, mixing and ascent. *Philosophical Trans. R. Soc. A Math. Phys. Eng. Sci.* 377, 20180004. doi:10.1098/rsta.2018.0004

Cashman, K. V., and Taggart, J. E. (1983). Petrologic monitoring of 1981 and 1982 eruptive products from Mount St. Helens. *Science* 221, 1385–1387. doi:10.1126/science.221.4618.1385

Cassidy, M., Manga, M., Cashman, K., and Bachmann, O. (2018). Controls on explosive-effusive volcanic eruption styles. *Nat. Commun.* 9, 2839. doi:10.1038/s41467-018-05293-3

Castro, J. M., and Feisel, Y. (2022). Eruption of ultralow-viscosity basanite magma at Cumbre Vieja, La Palma, Canary Islands. *Nat. Commun.* 13, 1–12. doi:10.1038/S41467-022-30905-4

Charco, M., González, P. J., Pallero, J. L. G., García-Cañada, L., del Fresno, C., and Rodríguez-Ortega, A. (2024). The 2021 La Palma (Canary Islands) Eruption Ending Forecast Through Magma Pressure Drop. *Geophys Res. Lett.* 51, 1–10. doi:10.1029/2023GL106885

Civico, R., Ricci, T., Scarlato, P., Taddeucci, J., Andronico, D., Del Bello, E., et al. (2022). High-resolution Digital Surface Model of the 2021 eruption deposit of Cumbre Vieja volcano, La Palma, Spain. *Sci. Data* 9, 1–7. doi:10.1038/s41597-022-01551-8

Corsaro, R. A., and Miraglia, L. (2022). Near real-time petrologic monitoring on volcanic glass to infer magmatic processes during the February–April 2021 paroxysms of the South-East Crater, Etna. *Front. Earth Sci. (Lausanne)* 10, 828026. doi:10.3389/feart.2022.828026

Day, J. M. D., Geiger, H., Troll, V. R., Perez-Torrado, F. J., Aulinas, M., Gisbert, G., et al. (2022a). Bouncing Spallation Bombs During the 2021 La Palma Eruption, Canary Islands, Spain. *Earth Sci. Syst. Soc.* 2, 10063. doi:10.3389/ESSS.2022.10063

Day, J. M. D., Troll, V. R., Aulinas, M., Deegan, F. M., Geiger, H., Carracedo, J. C., et al. (2022b). Mantle source characteristics and magmatic processes during the 2021 La Palma eruption. *Earth Planet Sci. Lett.* 597, 117793. doi:10.1016/J.EPSL.2022.117793

Dayton, K., Gazel, E., Wieser, P., Troll, V. R., Carracedo, J. C., La Madrid, H., et al. (2023). Deep magma storage during the 2021 La Palma eruption. *Sci. Adv.* 9, 1–7. doi:10.1126/sciadv.ade7641

Dayton, K., Gazel, E., Wieser, P. E., Troll, V. R., Carracedo, J. C., Aulinas, M., et al. (2024). Magmatic Storage and Volatile Fluxes of the 2021 La Palma Eruption. *Geochem. Geophys. Geosystems* 25, e2024GC011491. doi:10.1029/2024GC011491

De Luca, C., Valerio, E., Giudicepietro, F., Macedonio, G., Casu, F., and Lanari, R. (2022). Pre- and co-eruptive analysis of the September 2021 eruption at cumbre Vieja Volcano (La palma, Canary Islands) through DInSAR measurements and analytical modeling. *Geophys Res. Lett.* 49, e2021GL097293. doi:10.1029/2021GL097293

del Fresno, C., Cesca, S., Klügel, A., Domínguez Cerdeña, I., Díaz-Suárez, E. A., Dahm, T., et al. (2023). Magmatic plumbing and dynamic evolution of the 2021 La Palma eruption. *Nat. Commun.* 14:1, 1–11. doi:10.1038/s41467-023-35953-y

Di Paolo, F., Ledo, J., Ślęzak, K., Martínez van Dorth, D., Cabrera-Pérez, I., and Pérez, N. M. (2020). La Palma island (Spain) geothermal system revealed by 3D magnetotelluric data inversion. *Sci. Rep.* 10, 1–8. doi:10.1038/S41598-020-75001-Z

Dumont, M., Peltier, A., Roblin, E., Reninger, P. A., Barde-Cabusson, S., Finizola, A., et al. (2019). Imagery of internal structure and destabilization features of active volcano by 3D high resolution airborne electromagnetism. *Sci. Rep.* 9 (1), 1–11. doi:10.1038/s41598-019-54415-4

D'Auria, L., Koulakov, I., Prudencio, J., Cabrera-Pérez, I., Ibáñez, J. M., Barrancos, J., et al. (2022). Rapid magma ascent beneath La Palma revealed by seismic tomography. *Sci. Rep.* 12, 1–13. doi:10.1038/s41598-022-21818-9

Edmonds, M., Cashman, K. V., Holness, M., and Jackson, M. (2019). Architecture and dynamics of magma reservoirs. *Philosophical Trans. R. Soc. A Math. Phys. Eng. Sci.* 377, 20180298. doi:10.1098/rsta.2018.0298

Fabbrizio, A., Bamber, E. C., Michailidou, E., Romero, J. E., Arzilli, F., Bonechi, B., et al. (2023). Phase equilibrium experiments and thermodynamic simulations to constrain the pre-eruptive conditions of the 2021 Tajogaite eruption (Cumbre Vieja volcano, La Palma, Canary Islands). *J. Volcanol. Geotherm. Res.* 442, 107901. doi:10.1016/j.jvolgeores.2023.107901

Federico, C., Cocina, O., Gambino, S., Paonita, A., Branca, S., Coltelli, M., et al. (2023). Inferences on the 2021 ongoing volcanic unrest at Vulcano Island (Italy) through a comprehensive multidisciplinary surveillance network. *Remote Sens. (Basel)* 15, 1405. doi:10.3390/rs15051405

Felpeto, A., Molina-Arias, A. J., Quirós, F., Pereda, J., García-Cañada, L., and Díaz-Suárez, E. A. (2022). "Measuring the height of the eruptive column during the 2021 eruption of Cumbre Vieja (La Palma Island, Canary Islands)," Vienna, Austria: EGU General Assembly. 23–27 May 2022, EGU22-9419.

Fernández, J., Romero, R., Carrasco, D., Luzón, F., and Araña, V. (2002). InSAR volcano and seismic monitoring in Spain. Results for the period 1992-2000 and possible interpretations. *Opt. Lasers Eng.* 37, 285–297. doi:10.1016/S0143-8166(01)00085-9

Fernández, J., Escayo, J., Camacho, A. G., Palano, M., Prieto, J. F., Hu, Z., et al. (2022). Shallow magmatic intrusion evolution below La Palma before and during the 2021 eruption. *Sci. Rep.* 12, 1–18. doi:10.1038/S41598-022-23998-W

Fernández Santín, S., Hernán Requera, F., Navarro Falcones, L. F., and Pliego Dones, D. (1974). Petrographic study of basaltic materials emitted by Teneguía volcano (La Palma, Canary Islands, October 27th–November 19th, 1971). *Estud. Geol.*, 27–34.

Ferretti, A., Prati, C., and Rocca, F. (2001). Permanent scatterers in SAR interferometry. *IEEE Trans. Geoscience Remote Sens.* 39, 8–20. doi:10.1109/36.898661

Galipp, K., Klügel, A., and Hansteen, T. H. (2006). Changing depths of magma fractionation and stagnation during the evolution of an oceanic island volcano: La Palma (Canary Islands). *J. Volcanol. Geotherm. Res.* 155, 285–306. doi:10.1016/J.JVOLGEORES.2006.04.002

García-Yeguas, A., Ledo, J., Piña-Varas, P., Prudencio, J., Queralt, P., Marcuello, A., et al. (2017). A 3D joint interpretation of magnetotelluric and seismic tomographic models: the case of the volcanic island of Tenerife. *Comput. Geosci.* 109, 95–105. doi:10.1016/j.cageo.2017.08.003

Girona, T., and Costa, F. (2013). DIPRA: a user-friendly program to model multi-element diffusion in olivine with applications to timescales of magmatic processes. *Geochem. Geophys. Geosystems* 14, 422–431. doi:10.1029/2012GC004427

Goldman, R. T., Albright, J. A., Gravley, D. M., Grosfils, E. B., Gregg, P. M., and Hampton, S. J. (2022). Stress control of dike deflection and flank eruption at Akaroa Volcano, New Zealand. *J. Geophys Res. Solid Earth* 127, e2022JB024305. doi:10.1029/2022JB024305

González-García, D., Boulesteix, T., Klügel, A., and Holtz, F. (2023). Bubble-enhanced basanite–tephrite mixing in the early stages of the Cumbre Vieja 2021 eruption, La Palma, Canary Islands. *Sci. Rep.* 13, 1–15. doi:10.1038/s41598-023-41595-3

Gottsmann, J., Camacho, A. G., Martí, J., Wooller, L., Fernández, J., García, A., et al. (2008). Shallow structure beneath the Central Volcanic Complex of Tenerife from new gravity data: implications for its evolution and recent reactivation. *Phys. Earth Planet. Interiors* 168, 212–230. doi:10.1016/j.pepi.2008.06.020

GRAFCAN (2019). Estaciones GNSS de Canarias. Retrieved February 11, 2019. Available online at: https://idecan2.grafcan.es/ServicioWMS/GNSS?&SERVICE=WMS&SRS=EPSG:32628&VERSION=1.1.1&REQUEST=GetFeatureInfo&STYLES=&X=335&Y=225&BBOX=22699.458157305082,2953559.870667103,820419.5218426948,3307830.6493328963&WIDTH=1306&H. Available online at: https://idecan2.grafcan.es/ServicioWMS/GNSS?&SERVICE=WMS&SRS=EPSG:32628&VERSION=1.1.1&REQUEST=GetFeatureInfo&STYLES=&X=335&Y=225&BBOX=22699.458157305082,2953559.870667103,820419.5218426948,3307830.6493328963&WIDTH=1306&HEIGHT=580&QUERY_LAYERS=Estaciones&LAYERS=Estaciones&INFO_FORMAT=text/html&FORMAT=image/png (Accessed May 19, 2025).

Guillou, H., Carracedo, J. C., and Duncan, R. A. (2001). K–Ar, 40Ar–39Ar ages and magnetostratigraphy of Brunhes and Matuyama lava sequences from La Palma Island. *J. Volcanol. Geotherm. Res.* 106, 175–194. doi:10.1016/S0377-0273(00)00294-8

Hanssen, R. F. (2001). Radar interferometry. 2. doi:10.1007/0-306-47633-9

Hernandez-Pacheco, A., and Valls, M. C. (1982). The historic eruptions of La Palma Island (Canaries). *Arquipélago. Série Ciências Nat.* 3, 83–94. Available online at: http://hdl.handle.net/10400.3/4915 (Accessed May 19, 2025).

Hooper, A., Bekaert, D., Spaans, K., and Arikan, M. (2012). Recent advances in SAR interferometry time series analysis for measuring crustal deformation. *Tectonophysics* 514–517, 1–13. doi:10.1016/J.TECTO.2011.10.013

Hreinsdóttir, S., Sigmundsson, F., Roberts, M. J., Björnsson, H., Grapenthin, R., Arason, P., et al. (2014). Volcanic plume height correlated with magma-pressure change at Grímsvötn Volcano, Iceland. *Nat. Geosci.* 7, 214–218. doi:10.1038/NGEO2044

Ibarrola, E. (1974). Temporal modification of the basaltic materials from the 1971 eruption of the Teneguía volcano (La Palma, Canary Islands). *Estud. Geol.*, 49–58.

Kahl, M., Chakraborty, S., Costa, F., and Pompilio, M. (2011). Dynamic plumbing system beneath volcanoes revealed by kinetic modeling, and the connection to monitoring data: an example from Mt. Etna. *Earth Planet Sci. Lett.* 308, 11–22. doi:10.1016/j.epsl.2011.05.008

Kahl, M., Mutch, E. J. F., Maclennan, J., Morgan, D. J., Couperthwaite, F., Bali, E., et al. (2023). Deep magma mobilization years before the 2021 CE Fagradalsfjall eruption, Iceland. *Geology* 51, 184–188. doi:10.1130/G50340.1

Kähmen, H., and Faig, W. (1988). Surveying. *de Gruyter, Berlin Matthews, LH (1938). The humpback whale, Megaptera nodosa.'Discovery'Rep* 17, 7–92.

Kereszturi, G., and Németh, K. (2012). Monogenetic basaltic volcanoes: genetic classification, growth, geomorphology and degradation. *Updat. Volcanol. - New Adv. Underst. Volcan. Syst.* doi:10.5772/51387

Klügel, A., Schmincke, H. U., White, J. D. L., and Hoernle, K. A. (1999). Chronology and volcanology of the 1949 multi-vent rift-zone eruption on La Palma (Canary Islands). *J. Volcanol. Geotherm. Res.* 94, 267–282. doi:10.1016/S0377-0273(99)00107-9

Klügel, A., Hoernle, K. A., and Schmincke, H. (2000). The chemically zoned 1949 eruption on La Palma (Canary Islands): petrologic evolution and magma supply dynamics of a rift zone eruption. *J. Geophys Res.* 105, 5997–6016.

Klügel, A., Hansteen, T. H., and Galipp, K. (2005). Magma storage and underplating beneath Cumbre Vieja volcano, La Palma (Canary Islands). *Earth Planet Sci. Lett.* 236, 211–226. doi:10.1016/j.epsl.2005.04.006

Klügel, A., Galipp, K., Hoernle, K., Hauff, F., and Groom, S. (2017). Geochemical and volcanological evolution of la palma, Canary Islands. *J. Petrology* 58, 1227–1248. doi:10.1093/petrology/egx052

Lamolda, H., Felpeto, A., and Bethencourt, A. (2017). Time lag between deformation and seismicity along monogenetic volcanic unrest periods: the case of El Hierro Island (Canary Islands). *Geophys Res. Lett.* 44, 6771–6777. doi:10.1002/2017GL074494;CTYPE:STRING:JOURNAL

Larrea, P., Albert, H., Ubide, T., Costa, F., Colás, V., Widom, E., et al. (2021). From explosive vent opening to effusive outpouring: mineral constraints on magma dynamics and timescales at Paricutin monogenetic volcano. *J. Petrology* 62, 1–19. doi:10.1093/petrology/egaa112

le Maitre, R. W., Bateman, P., Dudek, A., Keller, J., Lameyre, J., le Bas, M. J., et al. (1989). *A classification of igneous rocks and glossary of terms: recommendations of the International Union of Geological Sciences subcommission on the systematic of igneous rocks*. Oxford: Blackwell Scientific.

Liu, E. J., Cashman, K. V., Miller, E., Moore, H., Edmonds, M., Kunz, B. E., et al. (2020). Petrologic monitoring at Volcán de Fuego, Guatemala. *J. Volcanol. Geotherm. Res.* 405, 107044. doi:10.1016/j.jvolgeores.2020.107044

Longpré, M. A., Tramontano, S., Pankhurst, M. J., Roman, D. C., Reiss, M. C., Cortese, F., et al. (2025). Shifting melt composition linked to volcanic tremor at Cumbre Vieja volcano. *Nat. Geosci.* 18, 175–183. doi:10.1038/s41561-024-01623-x

López Acevedo, F. J., and Pellicer Bautista, M. J. (2014). Uso de Sistemas de Información Geográfica para el cálculo del volumen de los materiales emitidos en la erupción de 1971 del volcán Teneguía (La Palma, Islas Canarias). *Geogaceta* 56, 59–62.

López, C., Benito-Saz, M. A., Martí, J., Del-Fresno, C., García-Cañada, L., Albert, H., et al. (2017). Driving magma to the surface: the 2011–2012 El Hierro Volcanic Eruption. *Geochem. Geophys. Geosystems* 18, 3165–3184. doi:10.1002/2017GC007023

Luhr, J. F., and Carmichael, I. S. E. (1990). Petrological monitoring of cyclical eruptive activity at Volcán Colima, México. *J. Volcanol. Geotherm. Res.* 42, 235–260. doi:10.1016/0377-0273(90)90002-w

Luhr, J. F., Simkin, T., and Cuasay, M. (1993). *Parícutin: the volcano born in a Mexican cornfield*. Phoenix, AZ: US Geoscience Press.

Malengreau, B., Lénat, J. F., and Froger, J. L. (1999). Structure of Reunion Island (Indian Ocean) inferred from the interpretation of gravity anomalies. *J. Volcanol. Geotherm. Res.* 88, 131–146. doi:10.1016/S0377-0273(98)00114-0

Mangler, M. F., Petrone, C. M., and Prytulak, J. (2022). Magma recharge patterns control eruption styles and magnitudes at Popocatépetl volcano (Mexico). *Geology* 50, 366–370. doi:10.1130/G49365.1

Mezcua, J., and Rueda, J. (2023). Seismic swarms and earthquake activity b-value related to the September 19, 2021, La Palma volcano eruption in Cumbre Vieja, Canary Islands (Spain). *Bull. Volcanol.* 85, 1–16. doi:10.1007/s00445-023-01646-z

Miller, C. A., Williams-Jones, G., Fournier, D., and Witter, J. (2017). 3D gravity inversion and thermodynamic modelling reveal properties of shallow silicic magma reservoir beneath Laguna del Maule, Chile. *Earth Planet Sci. Lett.* 459, 14–27. doi:10.1016/j.epsl.2016.11.007

Montesinos, F. G., Sainz-Maza, S., Gómez-Ortiz, D., Arnoso, J., Blanco-Montenegro, I., Benavent, M., et al. (2023). Insights into the magmatic feeding system of the 2021 eruption at cumbre vieja (La palma, Canary Islands) inferred from gravity data modeling. *Remote Sens. (Basel)* 15. doi:10.3390/rs15071936

Nagaoka, Y., Nishida, K., Aoki, Y., Takeo, M., and Ohminato, T. (2012). Seismic imaging of magma chamber beneath an active volcano. *Earth Planet Sci. Lett.* 333–334, 1–8. doi:10.1016/j.epsl.2012.03.034

Pankhurst, M. J., Morgan, D. J., Thordarson, T., and Loughlin, S. C. (2018). Magmatic crystal records in time, space, and process, causatively linked with volcanic unrest. *Earth Planet Sci. Lett.* 493, 231–241. doi:10.1016/j.epsl.2018.04.025

Paonita, A., Caracausi, A., Iacono-Marziano, G., Martelli, M., and Rizzo, A. (2012). Geochemical evidence for mixing between fluids exsolved at different depths in the magmatic system of Mt Etna (Italy). *Geochim. Cosmochim. Acta* 84, 380–394. doi:10.1016/J.GCA.2012.01.028

Petrone, C. M., and Mangler, M. F. (2021). Elemental diffusion chronostratigraphy: time-Integrated insights into the dynamics of plumbing systems. *Crustal Magmatic Syst. Evol. Anat. Archit. Physico-Chemical Process.*, 179–193. doi:10.1002/9781119564485.ch8

Re, G., Corsaro, R. A., D'Oriano, C., and Pompilio, M. (2021). Petrological monitoring of active volcanoes: a review of existing procedures to achieve best practices and operative protocols during eruptions. *J. Volcanol. Geotherm. Res.* 419, 107365. doi:10.1016/j.jvolgeores.2021.107365

Reath, K., Pritchard, M. E., Roman, D. C., Lopez, T., Carn, S., Fischer, T. P., et al. (2021). Quantifying eruptive and background seismicity, deformation, degassing, and thermal emissions at volcanoes in the United States during 1978–2020. *J. Geophys Res. Solid Earth* 126, 1–24. doi:10.1029/2021JB021684

Reubi, O., Blundy, J., and Pickles, J. (2019). "Petrological monitoring of Volcán de Colima magmatic system: the 1998 to 2011 activity," in *Volcán de Colima: portrait of a Persistently Hazardous Volcano*, 219–240.

Rizzo, A., Aiuppa, A., Capasso, G., Grassa, F., Inguaggiato, S., Longo, M., et al. (2008). The 5 April 2003 Paroxysm at Stromboli, a review of geochemical observations. *The Stromboli Volcano, Integrated Study 2002-2003 Eruption. AGU Geophys Monogr* 182, 347–358.

Romero, J. E., Burton, M., Cáceres, F., Taddeucci, J., Civico, R., Ricci, T., et al. (2022). The initial phase of the 2021 Cumbre Vieja ridge eruption (Canary Islands): products and dynamics controlling edifice growth and collapse. *J. Volcanol. Geotherm. Res.* 431, 107642. doi:10.1016/j.jvolgeores.2022.107642

Romero Ortiz, J. (1951). La erupcion del Nambroque en la Isla de La Palma. *Bol. Inst. Geol. Min. Esp.* 63, 3–163.

Romero Ruiz, M. D. C. (1990). Las manifestaciones volcánicas históricas del Archipiélago Canario. *Canary Isl. Spain Univ. La Laguna*. Available online at: https://riull.ull.es/xmlui/handle/915/10113. (Accessed Feburary 06, 2026)

Sandoval-Velasquez, A., Rizzo, A. L., Casetta, F., Ntaflos, T., Aiuppa, A., Alonso, M., et al. (2023). The noble gas signature of the 2021 Tajogaite eruption (La Palma, Canary Islands). *J. Volcanol. Geotherm. Res.* 443, 107928. doi:10.1016/j.jvolgeores.2023.107928

Saunders, K., Blundy, J., Dohmen, R., and Cashman, K. (2012). Linking petrology and seismology at an active volcano. *Science* 336, 1023–1027. doi:10.1126/science.1220066

Scarpa, R., Tilling, R. I., and Giggenbach, W. F. (1996). "Chemical composition of volcanic gases," in *Monitoring and mitigation of volcano hazards*, 221–256.

Scarrow, J. H., Pankhurst, M. J., Barbee, O. A., Chamberlain, K. J., Morgan, D. J., Longpré, M.-A., et al. (2024). Decoding links between magmatic processes and eruption dynamics: whole-rock time series petrology of the 2021 Tajogaite eruption, La Palma. *Volcanica* 7 (2), 953–980. doi:10.30909/vol.07.02.953980

Spina, L., Taddeucci, J., Cannata, A., Sciotto, M., Del Bello, E., Scarlato, P., et al. (2017). Time-series analysis of fissure-fed multi-vent activity: a snapshot from the July 2014 eruption of Etna volcano (Italy). *Bull. Volcanol.* 79, 1–12. doi:10.1007/S00445-017-1132-X/METRICS

Staudigel, H., and Schmincke, H. U. (1984). The Pliocene seamount series of La Palma/Canary Island. *J. Geophys Res.* 89, 11195–11215. doi:10.1029/JB089IB13P11195;CTYPE:STRING:JOURNAL

Staudigel, H., Feraud, G., and Giannerini, G. (1986). The history of intrusive activity on the island of La Palma (Canary Islands). *J. Volcanol. Geotherm. Res.* 27, 299–322. doi:10.1016/0377-0273(86)90018-1

Suarez, E. D., Domínguez-Cerdeña, I., Villaseñor, A., Aparicio, S. S. M., del Fresno, C., and García-Cañada, L. (2023). Unveiling the pre-eruptive seismic series of the La Palma 2021 eruption: insights through a fully automated analysis. *J. Volcanol. Geotherm. Res.* 444, 107946. doi:10.1016/J.JVOLGEORES.2023.107946

Taddeucci, J., Scarlato, P., Andronico, D., Ricci, T., Civico, R., Del Bello, E., et al. (2023). The Explosive Activity of the 2021 Tajogaite Eruption (La Palma, Canary Islands, Spain). *Geochem. Geophys. Geosystems* 24, e2023GC010946. doi:10.1029/2023GC010946

Tauxe, L., Staudigel, H., Wijbrans, J. R., Tauxe, L., Staudigel, H., and Wijbrans, J. R. (2000). Paleomagnetism and 40Ar/39Ar ages from La Palma in the Canary Islands. *Geochem. Geophys. Geosystems* 1. doi:10.1029/2000GC000063

Torres-González, P., Moure-García, D., Luengo-Oroz, N., Villasante-Marcos, V., Soler, V., Iribarren, I., et al. (2019). Spatial and temporal analysis of temperature and gaseous emission inside a gallery in an active volcanic Island (Tenerife, Canary Islands). *Pure Appl. Geophys*. doi:10.1007/s00024-019-02174-8

Torres-González, P. A., Luengo-Oroz, N., Lamolda, H., D'Alessandro, W., Albert, H., Iribarren, I., et al. (2020). Unrest signals after 46 years of quiescence at Cumbre Vieja, La Palma, Canary Islands. *J. Volcanol. Geotherm. Res.* 392, 106757. doi:10.1016/j.jvolgeores.2019.106757

Troll, V. R., Aulinas, M., Carracedo, J. C., Geiger, H., Perez-Torrado, F. J., Soler, V., et al. (2024a). The 2021 La Palma eruption: social dilemmas resulting from life close to an active volcano. *Geol. Today* 40, 96–111. doi:10.1111/GTO.12472

Troll, V. R., Deegan, F. M., Thordarson, T., Tryggvason, A., Krmíček, L., Moreland, W. M., et al. (2024b). The Fagradalsfjall and Sundhnúkur fires of 2021–2024: a single magma reservoir under the Reykjanes Peninsula, Iceland? *Terra Nova* 36, 447–456. doi:10.1111/TER.12733

Ubide, T., Mollo, S., Zhao, J., Nazzari, M., and Scarlato, P. (2019). Sector-zoned clinopyroxene as a recorder of magma history, eruption triggers, and ascent rates. *Geochim. Cosmochim. Acta* 251, 265–283. doi:10.1016/j.gca.2019.02.021

Ubide, T., Márquez, Á., Ancochea, E., Huertas, M. J., Herrera, R., Coello-Bravo, J. J., et al. (2023). Discrete magma injections drive the 2021 La Palma eruption. *Sci. Adv.* 9, eadg4813. doi:10.1126/sciadv.adg4813

Valentine, G. A., and Gregg, T. K. P. (2008). Continental basaltic volcanoes - processes and problems. *J. Volcanol. Geotherm. Res.* 177, 857–873. doi:10.1016/j.jvolgeores.2008.01.050

Wadsworth, F. B., Kennedy, B. M., Branney, M. J., von Aulock, F. W., Lavallée, Y., and Menendez, A. (2015). Exhumed conduit records magma ascent and drain-back during a Strombolian eruption at Tongariro volcano, New Zealand. *Bull. Volcanol.* 77, 1–10. doi:10.1007/S00445-015-0962-7/METRICS

Wegmüller, U., Werner, C., Strozzi, T., and Wiesmann, A. (2004). "Multi-temporal interferometric point target analysis," in *Analysis of multi-temporal remote sensing images*, World Scientific, 136–144.

Zanon, V., D'Auria, L., Schiavi, F., Cyrzan, K., and Pankhurst, M. J. (2024). Toward a near real-time magma ascent monitoring by combined fluid inclusion barometry and ongoing seismicity. *Sci. Adv.* 10, 1–14. doi:10.1126/sciadv.adi4300